

1 Using a Speed-Dependent Voigt Line Shape to Retrieve O₂ from 2 Total Carbon Column Observing Network Solar Spectra to Improve 3 Measurements of XCO₂

4 Authors: Joseph Mendonca¹, Kimberly Strong¹, Debra Wunch¹, Geoffrey C. Toon², David A.
5 Long³, Joseph T. Hodges³, Vincent T. Sironneau³, and Jonathan E. Franklin⁴.

6 1. Department of Physics, University of Toronto, Toronto, ON, Canada

7 2. Jet Propulsion Laboratory, Pasadena, CA, USA

8 3. National Institute of Standards and Technology, Gaithersburg, MD, USA

9 4. Harvard John A. Paulson School of Engineering and Applied Sciences, Cambridge, MA, USA

10 *Correspondence to:* Joseph Mendonca (joseph.mendonca@utoronto.ca)

11 **Abstract.** High-resolution, laboratory, absorption spectra of the $a^1\Delta_g \leftarrow X^3\Sigma_g^-$ oxygen (O₂) band measured using
12 cavity ring-down spectroscopy were fitted using the Voigt and speed-dependent Voigt line shapes. We found that
13 the speed-dependent Voigt line shape was better able to model the measured absorption coefficients than the Voigt
14 line shape. We used these line shape models to calculate absorption coefficients to retrieve atmospheric total
15 columns abundances of O₂ from ground-based spectra from four Fourier transform spectrometers that are part of
16 the Total Carbon Column Observing Network (TCCON) Lower O₂ total columns were retrieved with the speed-
17 dependent Voigt line shape, and the difference between the total columns retrieved using the Voigt and speed-
18 dependent Voigt line shapes increased as a function of solar zenith angle. Previous work has shown that carbon
19 dioxide (CO₂) total columns are better retrieved using a speed-dependent Voigt line shape with line mixing. The
20 column-averaged dry-air mole fraction of CO₂ (XCO₂) was calculated using the ratio between the columns of CO₂
21 and O₂ retrieved (from the same spectra) with both line shapes from measurements made over a one-year period at
22 the four sites. The inclusion of speed dependence in the O₂ retrievals significantly reduces the airmass dependence
23 of XCO₂ and the bias between the TCCON measurements and calibrated integrated aircraft profile measurements
24 was reduced from 1% to 0.4%. These results suggest that speed dependence should be included in the forward
25 model when fitting near-infrared CO₂ and O₂ spectra to improve the accuracy of XCO₂ measurements.

26 1. Introduction

27 Accurate remote sensing of greenhouse gases (GHGs), such as CO₂, in Earth's atmosphere is important for studying
28 the carbon cycle to better understand and predict climate change. The absorption of solar radiation by O₂ in the
29 Earth's atmosphere is important because it can be used to study the properties of clouds and aerosols, and to
30 determine vertical profiles of temperature and surface pressure. Wallace and Livingston (1990) were the first to
31 retrieve total columns of O₂ from some of the discrete lines of the $a^1\Delta_g \leftarrow X^3\Sigma_g^-$ band of O₂ centered at 1.27 μm
32 (which will be referred to below as the 1.27 μm band) using atmospheric solar absorption spectra from the Kitt

33 Peak observatory. Mlawer et al. (1998) recorded solar absorption spectra in the near-infrared (NIR) region to study
34 collision-induced absorption (CIA) in the $a^1\Delta_g \leftarrow X^3\Sigma_g^-$ band as well as two other O₂ bands. The spectra were
35 compared to a line-by-line radiative transfer model and the differences between the measured and calculated spectra
36 showed the need for better absorption coefficients in order to accurately model the 1.27 μm band (Mlawer et al.,
37 1998). Subsequently, spectroscopic parameters needed to calculate the absorption coefficients from discrete
38 transitions of the 1.27 μm band were measured in multiple studies (Cheah et al., 2000; Newman et al., 2000, 1999;
39 Smith and Newnham, 2000), as was collision-induced absorption (CIA) (Maté et al., 1999; Smith and Newnham,
40 2000), while Smith et al. (2001) validated the work done in Smith and Newnham (2000) using solar absorption
41 spectra.

42 The 1.27 μm band is of particular importance to the Total Carbon Column Observing Network (TCCON) (Wunch
43 et al., 2011). TCCON is a ground-based remote sensing network that makes accurate and precise measurements of
44 GHGs for satellite validation and carbon cycle studies. Using the O₂ column retrieved from solar absorption spectra,
45 the column-averaged dry-air mole fraction of CO₂ (XCO₂) has been shown to provide better precision than using the
46 surface pressure to calculate XCO₂ (Yang et al., 2002). The O₂ column is retrieved from the 1.27 μm band because
47 of its close proximity to the spectral lines used to retrieve CO₂, thereby reducing the impact of solar tracker mis-
48 pointing and an imperfect instrument line shape (ILS) (Washenfelder et al., 2006). To improve the retrievals of O₂
49 from the 1.27 μm band, Washenfelder et al. (2006) found that adjusting the spectroscopic parameters in HITRAN
50 2004 (Rothman et al., 2005) decreased the airmass and temperature dependence of the O₂ column. These revised
51 spectroscopic parameters were included in HITRAN 2008 (Rothman et al., 2009). Atmospheric solar absorption
52 measurements from this band made at the Park Falls TCCON site by Washenfelder et al. (2006) were the first
53 measurements to observe the electric-quadrupole transitions (Gordon et al., 2010). Leshchishina et al. (2011, 2010)
54 subsequently used cavity-ring-down spectra to retrieve spectroscopic parameters for the 1.27 μm band using a Voigt
55 spectral line shape and these parameters were included in HITRAN 2012 (Rothman et al., 2013). Spectroscopic
56 parameters for the discrete spectral lines of the O₂ 1.27 μm band from HITRAN 2016 (Gordon et al., 2017) are very
57 similar to HITRAN 2012 except that HITRAN2016 includes improved line positions reported by Yu et al. (2014).

58 Extensive spectral line shape studies have been performed for the O₂ A-band, which is centered at 762 nm and used
59 by the Greenhouse Gases Observing Satellite (GOSAT) (Yokota et al., 2009) and the Orbiting Carbon Observatory-
60 2 (OCO-2) satellite (Crisp et al., 2004) to determine surface pressure. Studies have shown that the Voigt line shape
61 is inadequate to describe the spectral line shape of the discrete O₂ lines in the A-band. Dicke narrowing occurs when
62 the motion of the molecule is diffusive due to collisions changing the velocity and direction of the molecule during
63 the time that it is excited. This diffusive motion is taken into account by averaging over many different Doppler
64 states resulting in a line width that is narrower than the Doppler width (Dicke, 1953). Long et al. (2010) and Predoi-
65 Cross et al. (2008) found it necessary to use a spectral Line shape model that accounted for Dicke narrowing when
66 fitting the discrete lines of the O₂ A-band. Line mixing, which occurs when collisions transfer intensity from one
67 part of the spectral band to another (Lévy et al., 1992), was shown to be prevalent in multiple studies (Predoi-Cross
68 et al., 2008; Tran et al., 2006; Tran and Hartmann, 2008). Tran and Hartmann (2008) showed that including line

69 mixing when calculating the O₂ A-band absorption coefficients reduced the airmass dependence of the O₂ column
 70 retrieved from TCCON spectra. When fitting cavity ring-down spectra of the O₂ A-band, Drouin et al. (2017) found
 71 it necessary to use a speed-dependence Voigt line shape, which takes into account different speeds at the time of
 72 collision (Shannon et al., 1986), with line mixing to properly fit the discrete spectral lines of the O₂ A-band.

73 The need to include non-Voigt effects when calculating absorption coefficients for the O₂ 1.27 μm band was first
 74 shown in Hartmann et al. (2013) and Lamouroux et al. (2014). In Hartmann et al. (2013) and Lamouroux et al.
 75 (2014), Lorentzian widths were calculated using the re-quantized classical molecular-dynamics simulations
 76 (rCMDs) and used to fit cavity-ring-down spectra with a Voigt line shape for some isolated transitions in the O₂
 77 1.27 μm band. The studies concluded that a Voigt line shape is insufficient for modeling the spectral lines of the O₂
 78 1.27 μm band and that effects such as speed dependence and Dicke narrowing should be included in the line shape
 79 calculation.

80 In this study, air-broadened laboratory cavity-ring-down spectra of the O₂ 1.27 μm band were fitted using a spectral
 81 line shape that takes into account speed dependence. The derived spectroscopic parameters for the speed-dependent
 82 Voigt line shape were used to calculate absorption coefficients when fitting high-resolution solar absorption spectra.
 83 Using these new O₂ total columns, and the simultaneously measured CO₂ total columns, using the updated line
 84 shape model described by Mendonca et al. (2016), to calculate XCO₂ and compared these results with XCO₂
 85 retrieved using a Voigt line shape. Section 2 details the formulas used to calculate absorption coefficients using
 86 different spectral line shapes. In Section 3, we describe the retrieval of spectroscopic parameters from three air-
 87 broadened cavity-ring-down spectra fitted with a speed-dependent Voigt line shape. For Section 4, the speed-
 88 dependent line shape along with the retrieved spectroscopic parameters is used to fit solar absorption spectra from
 89 four TCCON sites and retrieve total columns of O₂, which is compared to O₂ retrieved using a Voigt line shape. In
 90 Section 5, we investigate the change in the airmass dependence of XCO₂ with the new O₂ retrievals. In Section 6, we
 91 discuss our results and their implications for remote sensing of greenhouse gases.

92 **2. Absorption Coefficient Calculations**

93 **2.1 Voigt Line Shape**

94 The Voigt line shape is the convolution of the Lorentz and the Gaussian profiles, which model pressure and Doppler
 95 broadening of the spectral line respectively. The corresponding absorption coefficient, k , at a given wavenumber ν
 96 becomes :

$$k(\nu) = N \sum_j S_j \left(\frac{1}{\gamma_{Dj}} \right) \left(\frac{\ln(2)}{\pi} \right)^{1/2} \left(\text{Re}[c(\nu, x_j, y_j)] \right) \quad (1)$$

97 where N is the number density, S_j is the line intensity of spectral line j , γ_{Dj} is the Doppler half-width (HWHM), c is
 98 the complex error function, and

$$x_j = \frac{(v - v_j^o - P\delta_j^o)}{\gamma_{Dj}} (\ln(2))^{1/2}, \quad y_j = \frac{\gamma_{Lj}}{\gamma_{Dj}} (\ln(2))^{1/2}. \quad (2)$$

99 Here, v_j^o is the position of the spectral line j , P is the pressure, and δ_j^o is the pressure-shift coefficient. The Lorentz
100 half-width, γ_{Lj} , is calculated using:

$$\gamma_{Lj}(T) = P \gamma_{Lj}^o \left(\frac{296}{T} \right)^n \quad (3)$$

101 where γ_{Lj}^o is the air-broadened Lorentz half-width coefficient (at reference temperature 296 K) and n is the exponent
102 of temperature dependence. The Voigt line shape assumes that pressure broadening is accurately represented by a
103 Lorentz profile calculated for the stastical average velocity at the time of collision.

104 2.2 Speed-Dependent Voigt Line Shape

105 The speed-dependent Voigt line shape refines the pressure broadening component of the Voigt by calculating
106 multiple Lorentz profiles for different speeds at the time of collision. The final contribution from pressure
107 broadening to the speed-dependent Voigt is the weighted sum of Lorentz profiles (weighted by the Maxwell-
108 Boltzmann speed-distribution) calculated for different speeds at the time of collision. The speed-dependent Voigt
109 line shape (Ciuryło, 1998) with the quadratic representation of the Lorentz width and pressure shift (Rohart et al.,
110 1994) is:

$$k(v) = N \left(\frac{2}{\pi^{3/2}} \right) \sum_j S_j \int_{-\infty}^{\infty} e^{-v^2 V} \left(\tan^{-1} \left[\frac{x_j - B a_{\delta_j} (V^2 - 1.5) + V}{y_j (1 + a_{\gamma_{Lj}} (V^2 - 1.5))} \right] \right) dV \quad (4)$$

111 where $a_{\gamma_{Lj}}$ is the speed-dependent Lorentz width parameter (unitless) for line j , a_{δ_j} is the speed- dependent pressure-
112 shift parameter (unitless), B is $\frac{(\ln(2))^{1/2}}{\gamma_{Dj}}$, V is the ratio of the absorbing molecule's speed to the most probable speed
113 of the absorbing molecule, and all other variables are defined before.

114 3. Fitting Laboratory Spectra

115 O₂, unlike CO₂ and CH₄, cannot produce an electric dipole moment and therefore should not be infrared active.
116 However, O₂ has two unpaired electrons in the ground state that produce a magnetic dipole moment. Due to the
117 unpaired electrons in the ground state ($X^3\Sigma_g^-$) the rotational state (N) is split into three components which are given
118 by $J = N-1$, $J = N$, and $J = N+1$, while in the upper state ($a^1\Delta_g$), $J = N$. When labeling a transition, the following
119 nomenclature is used $\Delta N(N'')\Delta J(J'')$ (Leshchishina et al., 2010), where ΔN is the difference between N' in the upper
120 state and N'' in the lower state, ΔJ is the difference between J' in the upper state and J'' in the lower state. The
121 magnetic transitions of $a^1\Delta_g \leftarrow X^3\Sigma_g^-$ allow for $\Delta J=0, \pm 1$. This leads to 9 branches observed: P(N'')Q(J''),
122 R(N'')Q(J''), and Q(N'')Q(J''), for $\Delta J=0$, O(N'')P(J''), P(N'')P(J''), and Q(N'')P(J''), for $\Delta J=-1$, and S(N'')R(J''),
123 R(N'')R(J''), and Q(N'')R(J''), for $\Delta J=1$.

124 Absorption coefficients for three room temperature air-broadened (NIST Standard reference material® 2659a
125 containing 79.28 % N₂, 20.720(43) % O₂, 0.0029 % Ar, 0.00015 % H₂O, and 0.001 % other compounds) spectra
126 were measured at the National Institute of Standards and Technology (NIST) using the frequency-stabilized cavity-
127 ring-down spectroscopy (FS-CRDS)) technique (Hodges, 2005; Hodges et al., 2004). The absorption spectra were
128 acquired at pressures of 131 kPa, 99.3 kPa, and 66.9 kPa, at temperatures of 296.28 K, 296.34 K, and 296.30 K
129 respectively. Figure 1a shows the three measured absorption spectra. A more detailed discussion of the present FS-
130 CRDS spectrometer can be found in Lin et al. (2015).

131 The spectra were fitted individually using a Voigt line shape (Eq. 1), with S_j , $\gamma_{L_j}^o$, and δ_j^o for the main isotope of the
132 magnetic dipole lines of the O₂ 1.27 μm band for lines with an intensity greater than $7.0 \times 10^{-28} \text{ cm}^{-1}/(\text{molecule cm}^{-2})$.
133 The spectroscopic parameters measured in Leshchishina et al. (2011) for the spectral lines of interest were used as
134 the a priori for the retrieved spectroscopic parameters. The line positions were left fixed to the values measured in
135 Leshchishina et al. (2011), and all other O₂ spectral lines (intensity less $7.0 \times 10^{-28} \text{ cm}^{-1}/(\text{molecule cm}^{-2})$) were
136 calculated using a Voigt line shape with spectroscopic parameters from HITRAN 2012 (Rothman et al., 2013).
137 Spectral fits were done using the lsqnonlin function in Matlab, with a user-defined Jacobian matrix. The Jacobian
138 was constructed by taking the derivative of the absorption coefficients with respect to the parameters of interest.
139 Using an analytical Jacobian instead of the finite difference method is both computationally faster and more
140 accurate. The Voigt line shape was calculated using the Matlab code created by Abrarov and Quine (2011) to
141 calculate the complex error function and its derivatives. To take collision-induced absorption (CIA) into account, a
142 set of 50 Legendre polynomials were added together by retrieving the weighting coefficients needed to add the
143 polynomials to fit the CIA for each spectrum. Figure 1b shows the residual (measured minus calculated absorption
144 coefficients) when using a Voigt line shape with the retrieved spectroscopic parameters. The plot shows that residual
145 structure still remains for all three spectra. The Root Mean Square (RMS) residual values for the spectra are given
146 by the legend at the side of the plot.

147 Figure 2 is the same plot as Figure 1 but for the P(11)P(11), P(11)Q(10), P(9)P(9), and P(9)Q(8) spectral lines only.
148 Figure 2b shows that for all four spectral lines there is a “W” shaped residual at the line center. The P(11)P(11) line
149 was also measured by Hartmann et al. (2013) at pressures ranging from 6.7 to 107 kPa. Figure 5 of Hartmann et al.
150 (2013) shows the P(11)P(11) line at a pressure of 66.7 kPa, which is approximately the pressure of the 66.9 kPa
151 spectrum (blue spectrum in Figure 1 and 2). When one compares the blue residual of the P(11)P(11) line in Figure
152 2b to that of the residual of the left panel of Figure 5 of Hartmann et al. (2013), one can see that the residuals are the
153 same. Figure 6 of Hartmann et al. (2013) show that the amplitude of the residual increases with decreasing pressure,
154 which is also seen in Figure 2b. Figure 3 of Lamouroux et al. (2014) shows the same “W” residual for the P(9)P(9)
155 lines and that the amplitude of the residual increases with decreasing pressure (although for lower pressures)
156 consistent with the results for the P(9)P(9) line in Figure 2b.

157 Figure 1c shows the residual when using the speed-dependent Voigt (Eq. 4) to fit each spectrum individually. To use
158 Eq. (4) requires integration over all possible speeds, which is not computationally practical, so we employ the

159 simple numerical integration scheme as was done by Wehr (2005). When fitting the spectra, parameters S_j , $\gamma_{L_j}^o$, δ_j^o ,
160 $a_{\gamma_{L_i}}$ and a_{δ_j} were retrieved for lines of intensity greater than $7.0 \times 10^{-28} \text{ cm}^{-1}/(\text{molecule cm}^{-2})$, while all other O_2 lines
161 were calculated using a Voigt line shape and spectroscopic parameters from HITRAN 2012 (Rothman et al., 2013b).
162 The Jacobian matrix was created by taking the derivative with respect to each parameter of interest, as was done
163 with the Voigt fits. By taking speed-dependent effects into account, the residuals were reduced to 25 times smaller
164 than those for the Voigt fit and the RMS residuals (given in the legend of Figure 1c) are 10 times smaller. However,
165 some residual structure still remains, which is more evident in the in the Q and R branches than the P branch. Figure
166 2c shows the four lines in the P branch, as discussed when analyzing the Voigt fits. A small residual “W” remains at
167 line center, as well as residuals from weak O_2 lines.

168 Figure 3 shows the averaged intensity, Lorentz width coefficient, pressure shift coefficient, and speed-dependent
169 shift coefficient of the $1.27 \mu\text{m}$ O_2 band, retrieved from the three spectra, plotted as a function of quantum number
170 m which is $m=-J$ (where J is the lower state rotational quantum number) for the P-branch lines, $m=J$ for the Q-
171 branch lines, and $m=J+1$ for the R-branch lines. The intensity, Lorentz widths, and pressure shifts show a m
172 dependence for these parameters for the P and R sub-branches. The measured Lorentz widths and pressure shifts for
173 the Q sub-branches show a m dependence but are not as strong as the P and R sub-branches. This is because the Q
174 branch lines are broadened enough to blend with each other since they are spaced closer together than the P or R
175 branch lines. Figure 1c shows that some of the residual structure in the Q branch increases with pressure and is
176 partly due to the blending of these transitions as the pressure increases. The weak O_2 absorption lines also blend in
177 with the Q branch, contributing to the residual structure in Figure 1c. We tried retrieving the spectroscopic
178 parameters for the weak O_2 absorption lines, but since they were overlapping with the strong O_2 lines, it was not
179 possible. Figure 4a shows the retrieved speed-dependent width parameter averaged over the three spectra, plotted as
180 a function of m , showing that it increases with m . Error bars correspond to the 2σ standard deviation and are large
181 regardless of sub-branch. Figure 4b shows the retrieved speed-dependent width for the PQ sub-branch for the
182 different pressures. The speed-dependent width shows the same m dependence regardless of pressure, but also
183 increases with decreasing pressure as is the case for sub-branches. It should be noted that the speed-dependent width
184 parameter should be independent of pressure.

185 **4. Fitting Solar Spectra**

186 High-resolution solar absorption spectra were measured at four TCCON sites using a Bruker IFS 125HR FTIR
187 spectrometer with a room temperature InGaAs detector at a spectral resolution of 0.02 cm^{-1} (45 cm maximum
188 optical path difference). The raw interferograms recorded by the instrument were processed into spectra using the
189 I2S software package (Wunch, D. et al., 2015) that corrects solar intensity variations (Keppel-Aleks et al., 2007),
190 phase errors (Mertz, 1967), and laser sampling errors (Wunch, D. et al., 2015), and then performs a fast Fourier
191 transform to convert the interferograms into spectra (Bergland, 1969). The GGG software package (Wunch, D. et
192 al., 2015) is used to retrieve total columns of atmospheric trace gases. GFIT is the main code that contains the
193 forward model, which calculates a solar absorption spectrum using a line-by-line radiative transfer model and an
194 iterative non-linear least square fitting algorithm that scales an a priori gas profile to obtain the best fit to the

195 measured spectrum. A priori profiles for GHGs are created by an empirical model in GGG that is based on
196 measurements from the balloon-borne JPL MkIV Fourier Transform Spectrometer (FTS) (Toon, 1991), the
197 Atmospheric Chemistry Experiment (ACE) FTS instrument aboard SCISAT (Bernath et al., 2005), and in situ
198 GLOBALVIEW data (Wunch et al., 2011). Temperature and pressure profiles, as well as H₂O a priori profiles are
199 generated from the National Centers for Environmental Prediction (NCEP) data. The calculations are performed for
200 71 atmospheric layers (0 km to 70 km), so all a priori profiles are generated on a vertical grid of 1 km.

201 In the current GGG software package (Wunch, D. et al., 2015), the forward model of GFIT calculates absorption
202 coefficients for the discrete lines of the O₂ 1.27 μm band using a Voigt line shape and spectroscopic parameters
203 from Washenfelder et al. (2006a) and Gordon et al. (2010). To take CIA into account, absorption coefficients are
204 calculated using a Voigt line shape and spectroscopic parameters from the foreign-collision-induced absorption
205 (FCIA) and self-collision-induced absorption (SCIA) spectral line lists provided with the GGG software package
206 (Wunch, D. et al., 2015). Spectroscopic parameters in the FCIA and SCIA line lists were retrieved by Geoff Toon by
207 fitting the laboratory spectra of Smith and Newnham (2000). This was done by retrieving the integrated absorption
208 at every 1 cm⁻¹ of the spectrum and using a Voigt line shape, with fixed Lorentz width and no pressure shift. In
209 GFIT, a volume scale factor is retrieved for the CIA and discrete lines separately so that the O₂ column is derived
210 from the discrete lines of the 1.27 μm band only. Airglow is not considered when fitting the 1.27 μm band since the
211 spectrometer views the sun directly, and airglow is overwhelmed by such a bright source. The continuum level and
212 tilt of the 100% transmission level is fitted using a weighted combination of the first two Legendre polynomials.
213 Absorption coefficient for all other trace gases are calculated using a Voigt line shape and spectroscopic parameters
214 from the atm.101 line list (Toon, G. C., 2014a) and solar lines are fitted using the solar line list (Toon, G. C.,
215 2014b).

216 Figure 5 shows the spectral fit to a solar absorption spectrum recorded at Eureka on March 27, 2015, at a solar
217 zenith angle (SZA) of 81.32° (airmass of 6.3). This spectrum is an average of 5 Eureka scans. The TCCON standard
218 is single scan but 5 scans were averaged to decrease the noise. The measured spectrum (red circles), calculated
219 spectrum (black circles) and transitions from all gases in the window (colored lines, refer to the legend for different
220 gases) are shown in Figure 5b. The residual obtained using a Voigt line shape to calculate the discrete lines of the O₂
221 1.27 μm band is shown in red in Figure 5a. The blue residual is the result of using a speed-dependent Voigt line
222 shape with the spectroscopic parameters retrieved from fitting the absorption coefficients in Section 3. To decrease
223 the amount of time it takes to calculate the absorption coefficients, the quadratic-Speed Dependent Voigt (qSDV)
224 computational approach of Ngo et al. (2013) and Tran et al. (2013) was used instead of Eq. (4) since it requires the
225 Voigt calculation only twice, while Eq. (4) requires numerical integration scheme with 33 iterations. The
226 temperature-dependent parameter of the Lorentz width of the discrete lines of the O₂ 1.27 μm band reported in
227 HITRAN 2012 was used to take temperature dependence into account for $\gamma_{L_j}(T)$. There was only a slight
228 improvement in the fit residuals with the new absorption coefficients (using the qSDV), as seen in Figure 5a.
229 Absorption coefficients calculated with the qSDV were used to retrieve total columns of O₂ from solar spectra
230 recorded over a one year period at TCCON sites in Eureka (eu) (Nunavut, Canada) (Batchelor et al., 2009; Strong et

231 al., 2017), Park Falls (pa) (Wisconsin, U.S.A) (Washenfelder et al., 2006; Wennberg et al., 2017) , Lamont (oc)
232 (Oklahoma, U.S.A) (Wennberg et al., 2017b), and Darwin (db) (Australia) (Deutscher et al., 2010; Griffith et al.,
233 2017). In total 131 124 spectra were fitted using the qSDV and the average root mean square (RMS) residual of the
234 fit only decreased by 0.5 %.

235 **5. Impact of O₂ Columns on XCO₂ Measurements**

236 The O₂ column retrieved from the 1.27 μm band with a Voigt line shape and spectroscopic parameters from the
237 atm.101 line list (Toon, G. C., 2014a) has an airmass dependence such that the O₂ column retrieved increases as a
238 function of solar zenith angle (or airmass). Using spectra recorded from Eureka, Park Falls, Lamont, and Darwin
239 over one-year periods, total columns of O₂ were retrieved using (1) a Voigt spectral line shape with spectroscopic
240 parameters from the atm.101 line list and (2) the qSDV with the spectroscopic parameters determined in Section 3.
241 Figure 6 shows the percent difference calculated as the column from the qSDV retrieval minus the column from the
242 Voigt retrieval, which was then divided by the latter and multiplied by 100, plotted as a function of solar zenith
243 angle (SZA). At the smallest SZA, the qSDV retrieves 0.75% less O₂ than the Voigt, with the difference increasing
244 to approximately 1.8% as the SZA approaches 90°. Figure 7 shows XAIR for the entire data set plotted as a function
245 of SZA. XAIR is the column of air (determined using surface pressure recorded at the site) divided by the column of
246 O₂ retrieved from the spectra and multiplied by 0.2095, which is the dry air mole fraction of O₂ in Earth's
247 atmosphere. Ideally XAIR should be 1 but when using O₂ retrieved with a Voigt line shape (Figure 7a) to calculate
248 XAIR the average XAIR value for the entire data set is 0.977. Using O₂ retrieved with the qSDV, to calculate XAIR
249 the average value is 0.986 which is closer to the expected value of 1. However, XAIR has a dependence on SZA
250 regardless of line shape used. Figure 7a shows that XAIR decreases as a function of SZA (evident at SZA > 75°)
251 which means that the retrieved column of O₂ increases as a function of SZA. Figure 7b shows that XAIR increases
252 as a function of SZA (evident at SZA > 70°), which means that the retrieved column of O₂ decreases as a function of
253 SZA. Therefore retrieving total columns of O₂ with the qSDV changes the airmass dependence of the O₂ column
254 which in turn will impact the airmass dependence of XCO₂.

255 **5.1 Airmass Dependence of XCO₂**

256 Since the standard TCCON XCO₂ (and all other XGases) is calculated using the column of O₂ instead of the surface
257 pressure, errors associated with the retrieval of O₂, such as the airmass dependence of the O₂ column, will affect
258 XCO₂. Figure 8 is XCO₂ calculated for four different combinations pertaining to the two CO₂ column retrievals and
259 the O₂ column retrievals. The CO₂ columns were retrieved with either a Voigt line shape (the standard GGG2014
260 approach) or the qSDV with line mixing as done in Mendonca et al. (2016) while the O₂ columns were retrieved
261 with either a Voigt (the standard GGG2014 approach) or the new qSDV approach developed here. Figure 8 shows a
262 spurious symmetric component to XCO₂ when the total column of O₂ is retrieved with the Voigt line shape,
263 regardless of line shape used to retrieve CO₂. When the qSDV is used to retrieve total columns of O₂, the symmetric
264 component of XCO₂ is dismissed regardless of line shape used to retrieve CO₂. This is because the airmass
265 dependence of the column of O₂ retrieved using the qSDV is more consistent with the airmass dependence of the

266 column of CO₂ (for both line shapes used to retrieve CO₂). Mendonca et al. (2016) showed that using the qSDV with
 267 line mixing results in better fits to the CO₂ windows and impacts the airmass dependence of the retrieved column of
 268 CO₂. When using a Voigt line shape the retrieved column amount of CO₂ decreases as airmass increases until the
 269 airmass is large (SZA of about 82°) at which point the retrieved column of CO₂ increases as the airmass increases,
 270 changing the shape of the airmass dependence of the CO₂ column. When the qSDV with line mixing is used, the
 271 retrieved column of CO₂ decreases as a function of airmass (up until the sun is above the horizon).

272 To correct for this, an empirical correction is applied to all TCCON XCO₂ (and XGas). The empirical correction
 273 determines the antisymmetrical component of the day's XCO₂, which is assumed to be the true variation of XCO₂
 274 throughout the day, as well as the symmetrical component, which is caused by the airmass dependence of the
 275 retrieved column of the gas of interest and O₂. We can, therefore, represent a measurement as (Wunch et al., 2011):

$$y_i = \hat{y}[1 + \alpha S(\theta_i) + \beta A(t_i)] \quad (5)$$

276 where \hat{y} is the mean value of XCO₂ measured that day, β is the fitted coefficient of the antisymmetric function $A(t_i)$
 277 and α is the fitted coefficient of the symmetric function $S(\theta_i)$. The antisymmetric function is calculated by (Wunch
 278 et al., 2011):

$$A(t_i) = \sin(2\pi(t_i - t_{noon})) \quad (6)$$

279 where t_i is the time of the measurement and t_{noon} is the time at solar noon, both in units of days. The symmetric
 280 function is calculated by (Wunch et al., 2011):

$$S(\theta_i) = \left(\frac{\theta_i + 13^\circ}{90^\circ + 13^\circ}\right)^3 - \left(\frac{45^\circ + 13^\circ}{90^\circ + 13^\circ}\right)^3 \quad (7)$$

281 where θ_i is the SZA in degrees. To determine α for the different line shapes, total columns of CO₂ were retrieved
 282 using the Voigt line shape (Wunch, D. et al., 2015) and the qSDV with line mixing (Mendonca et al., 2016).
 283 Henceforth, we will refer to XCO₂ calculated from O₂ and CO₂ using the Voigt line shape as XCO₂ Voigt and the
 284 qSDV line shape as XCO₂ qSDV.

285 Figure 9 shows the average α calculated for each season at Darwin, Lamont, and Park Falls. Eureka XCO₂ cannot be
 286 used to determine α because Eureka measurements do not go through the same range of SZAs as the other three
 287 sites due to its geolocation. The average α values derived from XCO₂ Voigt are represented by stars in Figure 9,
 288 while the squares indicate XCO₂ qSDV. At all three sites, α is closer to 0 when the qSDV line shape is used in the
 289 retrieval compared to the Voigt retrieval, regardless of the season. The average α for XCO₂ Voigt calculated from a
 290 year of measurements from Darwin, Park Falls, and Lamont is -0.0071 ± 0.0057 and that for XCO₂ qSDV is -
 291 0.0012 ± 0.0054 .

292 For all four sites, $\alpha = -0.0071$ is used to correct XCO₂ Voigt measurements. Figure 10a shows the XCO₂ Voigt
 293 anomalies plotted as a function of SZA. The data is expressed as the daily XCO₂ anomaly, which is the difference

294 between the XCO₂ value and the daily median value, in order to remove the seasonal cycle. When XCO₂ is left
295 uncorrected for airmass dependencies, XCO₂ decreases as a function of SZA up to approximately 82°, and increases
296 as a function of SZA at angles greater than 82°. Figure 10b shows XCO₂ Voigt corrected for the airmass
297 dependence. This airmass correction works well only up to a SZA of approximately 82°. Figure 10c is the same as
298 10a but for the uncorrected XCO₂ qSDV measurements, while Figure 10d is the same as 10b but for the corrected
299 XCO₂ qSDV measurements. When the airmass correction is applied to XCO₂ qSDV there is a small difference
300 between the corrected and uncorrected XCO₂ qSDV measurements, with the difference only noticeable for the
301 Darwin measurements recorded at SZA > 60°. For XCO₂ qSDV measurements made at SZA > 82° XCO₂ does not
302 increase with SZA as it does with the Voigt.

303 **5.2 Accuracy of XCO₂**

304 To assess the accuracy of TCCON XCO₂ measurements, they are compared to aircraft XCO₂ profile measurements
305 using the method described in Wunch et al. (2010). Figure 11a shows the comparison between the aircraft XCO₂
306 (Deutscher et al., 2010; Lin et al., 2006; Messerschmidt et al., 2010; Singh et al., 2006; Wofsy, 2011) measurements
307 (legend at the top details the different aircraft) and TCCON XCO₂ Voigt measurements for 13 TCCON sites (given
308 by the color-coded legend at the bottom right). The gray line indicates the one-to-one line and the dashed line is the
309 line of best fit. There is a bias of 0.9897 ± 0.0005 , as given by the slope of the line of best fit in Figure 11a, for the
310 XCO₂ Voigt measurements. Figure 11b is the same as 11a but for the XCO₂ qSDV measurements. The bias between
311 the aircraft XCO₂ measurements and the XCO₂ qSDV measurements is 1.0041 ± 0.0005 as given by the slope of the
312 line of best fit in Figure 11b. This increase in the slope can be explained by an increase in the retrieved column of
313 CO₂ when using the qSDV with line mixing as shown in Mendonca et al. (2016) as well as combined with a
314 decrease in the retrieved O₂ column due to using the qSDV. As discussed previously (section 5) the decrease in the
315 retrieved O₂ column is an improvement but the expected column of O₂ is still approximately 1.2% higher (at the
316 smallest SZA) than it should be. Therefore, the retrieved column of CO₂ is higher than it should be, and the slope
317 would be greater if the retrieved column of O₂ was 1.2% lower. Never the less using the qSDV to retrieve total
318 columns of CO₂ and O₂ reduces the difference between TCCON XCO₂ and aircraft XCO₂ measurements by 0.62 %.

319 TCCON XCO₂ measurements are divided by the scale factors (or bias determined in Figure 11) to calibrate to the
320 WMO scale. For all TCCON XCO₂ measurements retrieved with a Voigt line shape, the airmass correction is first
321 applied to the data and the result is divided by the determined bias factor, 0.9897. Figure 12a to 12d shows XCO₂
322 Voigt (for Eureka, Park Falls, Lamont, and Darwin respectively) indicated by red square boxes in the plots. XCO₂
323 Voigt measurements made at SZA > 82° have been filtered out because they cannot be corrected for the airmass
324 dependence. The blue boxes are XCO₂ qSDV corrected for airmass dependence and scaled by 1.0041. No filter was
325 applied to the XCO₂ qSDV measurements for SZA since the airmass dependence correction works at all SZA.
326 Figure 12e to 12h shows the difference between XCO₂ Voigt and XCO₂ qSDV for Eureka, Park Falls, Lamont, and
327 Darwin respectively. The mean differences for the data shown in Figures 12e to 12h are 0.113 ± 0.082 , -0.102 ± 0.223 ,
328 -0.132 ± 0.241 , and -0.059 ± 0.231 $\mu\text{mol/mol}$ (ppm) for Eureka, Park Falls, Lamont, and Darwin respectively. The

329 difference throughout the day at Park Falls, Lamont, and Darwin varies between -0.6 to 0.2 $\mu\text{mol/mol}$ and is SZA
330 dependent.

331 Figure 13a shows XCO_2 Voigt corrected for the airmass dependence, as well as XCO_2 qSDV, uncorrected and
332 corrected for the airmass dependence. These XCO_2 measurements were retrieved from Park Falls spectra recorded
333 on June 18, 2013. For all three XCO_2 measurements, the amount of XCO_2 decreases throughout the day. Figure 13b
334 shows the difference between the corrected Voigt XCO_2 and the uncorrected qSDV XCO_2 , as well as the difference
335 between the corrected Voigt XCO_2 and the corrected qSDV XCO_2 . The difference between the Voigt and the qSDV
336 (corrected and uncorrected) shows that at the start and end of the day, more XCO_2 is retrieved with the qSDV, while
337 at midday less is retrieved with the qSDV. The range in the differences seen in Figure 12e to 12h varies with SZA
338 throughout the day as shown in Figure 13b.

339 **6. Discussion and Conclusions**

340 Using cavity ring-down spectra measured in the lab, we have shown that the Voigt line shape is insufficient to
341 model the line shape of O_2 for the 1.27 μm band, consistent with the results of (Hartmann et al. (2013) and
342 Lamouroux et al. (2014). By using the speed-dependent Voigt line shape when calculating the absorption
343 coefficients, we were better able to reproduce the measured absorption coefficients than using the Voigt line shape.
344 However, some residual structure remains as seen Figures 1 and 2. This is partly due to the blending of spectral lines
345 (i.e., line mixing) and the inability to retrieve the spectroscopic parameters for weak O_2 transitions. Fitting low-
346 pressure spectra would help with isolating spectral lines and decreasing the uncertainty on the retrieved
347 spectroscopic parameters for the Q branch lines.

348 Accurate measurements of the pressure shifts in the 1.27 μm band have been hard to obtain as shown in Newman et
349 al. (1999) and Hill et al., (2003). While the retrieved pressure shifts show a dependence on quantum number m
350 (Figure 3c) as one would expect, this dependence is not as strong as the m dependence of the Lorentz widths (Figure
351 3b). This can be explained by the fact that line mixing, which is shown to be important for the O_2 A-band, was not
352 considered when fitting the cavity-ringdown spectra. Neglecting line mixing usually produces an asymmetric
353 residual in the discrete lines as well as a broad residual feature associated with the fact that collisions are transferring
354 intensity from one part of the spectrum to another. By fitting a set of Legendre polynomials for CIA we could be
355 simultaneously fitting the broader band feature associated with line mixing while the retrieved pressure shifts, and
356 speed-dependent pressure shifts could be compensating for the asymmetric structure one would see in the discrete
357 lines when neglecting line mixing. The remaining structure, as seen in Figure 1c, could be due to neglecting line
358 mixing especially in the Q-branch where the spacing between spectral lines is small (in comparison to the P and R
359 branches) and line mixing is most likely prevalent. The large error bars for the measured pressure shifts and speed-
360 dependent pressure shifts as well as a deviation from a smooth m dependence of these parameters could be due to
361 neglecting line mixing when fitting the lab spectra. Figure 3c and 3d show that the spectral lines that have large error
362 bars and deviate from an expected m dependence belong mainly to the Q-branch spectral lines (which are mostly
363 likely impacted by line mixing). To achieve the results obtained in this study it is best to use the parameters as is

364 instead of trying to apply an interpolation, that depends on m , or even omitting them unless one test's these changes
365 on atmospheric spectra that cover different range of conditions (i.e. seasons, dry/wet, SZA, geographical locations).
366 It is evident that the parameters might be compensating for affects (such as line mixing) that were not included when
367 fitting the lab spectra and changing these parameters (or omitting them) could lead to degradation in the quality of
368 the spectral fits of solar spectra and change the airmass dependence of the retrieved column of O_2 which would
369 impact the airmass dependence of XCO_2 .

370 The pressure dependence of the retrieved speed-dependent width parameter is an indication that Dicke narrowing
371 needs to be taken into account, as shown by Bui et al. (2014) for CO_2 . When both speed dependence and Dicke
372 narrowing are present, a multi-spectrum fit needs to be used due to the correlation between the parameters (Bui et
373 al., 2014). Domysławska et al. (2016) recommend using the qSDV to model the line shape of O_2 based on multiple
374 line shape studies of the O_2 B-band. In these studies, a multi-spectrum fit to low pressure (0.27-5.87 kPa) cavity-ring
375 down spectra was preformed testing multiple line shapes that took speed-dependence and Dicke narrowing into
376 account both separately and simultaneously. They found that the line shapes that only used Dicke narrowing were
377 not good enough to model the line shape of the O_2 B-band lines, but a line shape that included either speed-
378 dependence or both speed-dependence and Dicke narrowing produced similar quality fits, ultimately concluding that
379 speed-dependence has a larger effect than Dicke narrowing. It was noted in the study by Wójtewicz et al., (2014)
380 that both Dicke narrowing and speed-dependent effects might simultaneously play an important role in modeling the
381 line shape of the O_2 B-band lines. However, the speed-dependent and Dicke narrowing parameters are highly
382 correlated at low pressures. To reduce the correlation requires either a multi-spectrum fit of spectra at low pressures
383 with high enough signal to noise ratio or spectra that cover a wide range of pressure (Wójtewicz et al., 2014). So, by
384 combining the high-pressure spectra used in this study with low pressure spectra in a multispectrum fit both the
385 speed-dependence and Dicke narrowing parameters could be retrieved. The temperature dependence of the Lorentz
386 width coefficients of this band has never been measured before, which could have an impact on the airmass
387 dependence of O_2 . Combining high-pressure cavity-ring-down absorption coefficient measurements with those for
388 low pressures and different temperatures as done in Devi et al. (2015 and 2016) for CH_4 would lead to more accurate
389 line shape parameters for O_2 .

390 By taking speed dependence into account for both CO_2 (in the work of Mendonca et al., 2016) and O_2 (the work
391 presented here), we were able to significantly decrease the airmass dependence of TCCON XCO_2 and the bias
392 between TCCON and aircraft XCO_2 . XAIR calculated with the column of O_2 retrieved with the qSDV is now closer
393 to the expected value of 1 but XAIR still has an airmass dependence which is the results of the retrieved total
394 column of O_2 decreasing as a function of SZA at large SZA. This remaining airmass dependence could be due to
395 neglecting affects such as Dicke narrowing and line mixing in the absorption coefficient calculations, as well as
396 assuming a perfect instrument line shape in the retrieval algorithm. However, retrieving O_2 with the qSDV
397 significantly decreases the airmass dependence of XCO_2 . With the qSDV line shape, XCO_2 measurements made at
398 $SZA > 82^\circ$ no longer have to be discarded. We recommend using the full range of SZA which would result in more
399 XCO_2 measurement available from all TCCON sites. This is particularly important for high-latitude TCCON sites,

400 such as Eureka, because measurements made from late February to late March and from late September until mid-
401 October are made at $SZA > 82^\circ$. Filtering out these large SZA measurements thus limits the knowledge of the
402 seasonal cycle of XCO_2 at high latitudes. The airmass dependence of the O_2 column not only effects XCO_2 but all
403 trace gases measured by TCCON and in the future the airmass dependence of all XGas will be determined with
404 these new O_2 columns.

405 **Acknowledgements**

406 This work was primarily supported by the Canadian Space Agency (CSA) through the GOSAT and CAFTON
407 projects and the Natural Sciences and Engineering Research Council of Canada (NSERC). The Eureka
408 measurements were made at the Polar Environment Atmospheric Research Laboratory (PEARL) by the Canadian
409 Network for the Detection of Atmospheric Change (CANDAC), which has been supported by the AIF/NSRIT, CFI,
410 CFCAS, CSA, Environment Canada (EC), Government of Canada IPY funding, NSERC, OIT, ORF, PCSP, and
411 FQRNT. The authors wish to thank the staff at EC's Eureka Weather Station and CANDAC for the logistical and
412 on-site support provided. Thanks to CANDAC Principal Investigator James R. Drummond, PEARL Site Manager
413 Pierre Fogal, and CANDAC/PEARL operators Mike Maurice and Peter McGovern, for their invaluable assistance in
414 maintaining and operating the Bruker 125HR. The research at the Jet Propulsion Laboratory (JPL), and California
415 Institute of Technology was performed under contracts and cooperative agreements with the National Aeronautics
416 and Space Administration (NASA). Geoff Toon and Debra Wunch acknowledge support from NASA for
417 the development of TCCON via grant number NNX17AE15G. Darwin TCCON measurements are possible thanks
418 to support from NASA grants NAG5-12247 and NNG05-GD07G, the Australian Research Council grants
419 DP140101552, DP110103118, DP0879468 and LP0562346, and the DOE ARM program for technical support. The
420 research at the National Institute of Standards and Technology was performed with the support of the NIST
421 Greenhouse Gas Measurements and Climate Research Program. Certain commercial equipment, instruments, or
422 materials are identified in this paper in order to specify the experimental procedure adequately. Such identification is
423 not intended to imply recommendation or endorsement by the National Institute of Standards and Technology, nor is
424 it intended to imply that the materials or equipment identified are necessarily the best available for the purpose.

425

426

427

428

429

430

431

432 **References**

- 433 Abrarov, S.M., Quine, B.M.: Efficient algorithmic implementation of the Voigt/complex error function based on
434 exponential series approximation. *Appl. Math. Comput.* 218, 1894–1902.
435 <https://doi.org/10.1016/j.amc.2011.06.072>, 2011.
- 436 Batchelor, R.L., Strong, K., Lindenmaier, R., Mittermeier, R.L., Fast, H., Drummond, J.R., Fogal, P.F.: A New
437 Bruker IFS 125HR FTIR Spectrometer for the Polar Environment Atmospheric Research Laboratory at
438 Eureka, Nunavut, Canada: Measurements and Comparison with the Existing Bomem DA8 Spectrometer. *J.*
439 *Atmospheric Ocean. Technol.* 26, 1328–1340. <https://doi.org/10.1175/2009JTECHA1215.1>, 2009.
- 440 Bergland, G.: A radix-eight fast Fourier transform subroutine for real-valued series. *IEEE Trans. Audio*
441 *Electroacoustics* 17, 138–144. <https://doi.org/10.1109/TAU.1969.1162043>, 1969.
- 442 Bernath, P.F., McElroy, C.T., Abrams, M.C., Boone, C.D., Butler, M., Camy-Peyret, C., Carleer, M., Clerbaux, C.,
443 Coheur, P.-F., Colin, R., DeCola, P., DeMazière, M., Drummond, J.R., Dufour, D., Evans, W.F.J., Fast, H.,
444 Fussen, D., Gilbert, K., Jennings, D.E., Llewellyn, E.J., Lowe, R.P., Mahieu, E., McConnell, J.C.,
445 McHugh, M., McLeod, S.D., Michaud, R., Midwinter, C., Nassar, R., Nichitiu, F., Nowlan, C., Rinsland,
446 C.P., Rochon, Y.J., Rowlands, N., Semeniuk, K., Simon, P., Skelton, R., Sloan, J.J., Soucy, M.-A., Strong,
447 K., Tremblay, P., Turnbull, D., Walker, K.A., Walkty, I., Wardle, D.A., Wehrle, V., Zander, R., Zou, J.:
448 Atmospheric Chemistry Experiment (ACE): Mission overview. *Geophys. Res. Lett.* 32, L15S01.
449 <https://doi.org/10.1029/2005GL022386>, 2005.
- 450 Bui, T.Q., Long, D.A., Cygan, A., Sironneau, V.T., Hogan, D.W., Rupasinghe, P.M., Ciuryło, R., Lisak, D.,
451 Okumura, M.: Observations of Dicke narrowing and speed dependence in air-broadened CO₂ lineshapes
452 near 2.06 μm. *J. Chem. Phys.* 141, 174301. <https://doi.org/10.1063/1.4900502>, 2014.
- 453 Cheah, S.-L., Lee, Y.-P., Ogilvie, J.F.: Wavenumbers, strengths, widths and shifts with pressure of lines in four
454 bands of gaseous ¹⁶O₂ in the systems a¹Δ_g-X³Σ_g⁻ and b¹Σ_g⁺-X³Σ_g⁻. *J. Quant. Spectrosc. Radiat. Transf.*
455 64, 467–482. [https://doi.org/10.1016/S0022-4073\(99\)00126-0](https://doi.org/10.1016/S0022-4073(99)00126-0), 2000.
- 456 Ciuryło, R.: Shapes of pressure- and Doppler-broadened spectral lines in the core and near wings. *Phys. Rev. A* 58,
457 1029–1039. <https://doi.org/10.1103/PhysRevA.58.1029>, 1998.
- 458 Crisp, D., Atlas, R.M., Breon, F.-M., Brown, L.R., Burrows, J.P., Ciaï, P., Connor, B.J., Doney, S.C., Fung, I.Y.,
459 Jacob, D.J., Miller, C.E., O'Brien, D., Pawson, S., Randerson, J.T., Rayner, P., Salawitch, R.J., Sander,
460 S.P., Sen, B., Stephens, G.L., Tans, P.P., Toon, G.C., Wennberg, P.O., Wofsy, S.C., Yung, Y.L., Kuang, Z.,
461 Chudasama, B., Sprague, G., Weiss, B., Pollock, R., Kenyon, D., Schroll, S.: The Orbiting Carbon
462 Observatory (OCO) mission. *Adv. Space Res., Trace Constituents in the Troposphere and Lower*
463 *Stratosphere* 34, 700–709. <https://doi.org/10.1016/j.asr.2003.08.062>, 2004.
- 464 Deutscher, N.M., Griffith, D.W.T., Bryant, G.W., Wennberg, P.O., Toon, G.C., Washenfelder, R.A., Keppel-Aleks,
465 G., Wunch, D., Yavin, Y., Allen, N.T., Blavier, J.-F., Jiménez, R., Daube, B.C., Bright, A.V., Matross,
466 D.M., Wofsy, S.C., Park, S.: Total column CO₂ measurements at Darwin, Australia – site description and
467 calibration against in situ aircraft profiles. *Atmos Meas Tech* 3, 947–958. [https://doi.org/10.5194/amt-3-](https://doi.org/10.5194/amt-3-947-2010)
468 [947-2010](https://doi.org/10.5194/amt-3-947-2010), 2010.
- 469 Devi, V.M., Benner, D.C., Sung, K., Brown, L.R., Crawford, T.J., Yu, S., Smith, M.A.H., Mantz, A.W., Boudon,
470 V., Ismail, S.: Spectral line parameters including line shapes in the 2ν₃ Q branch of ¹²CH₄. *J. Quant.*
471 *Spectrosc. Radiat. Transf., XVIIIth Symposium on High Resolution Molecular Spectroscopy (HighRus-*
472 *2015)*, Tomsk, Russia 177, 152–169. <https://doi.org/10.1016/j.jqsrt.2015.12.009>, 2016.
- 473 Devi, V.M., Benner, D.C., Sung, K., Crawford, T.J., Yu, S., Brown, L.R., Smith, M.A.H., Mantz, A.W., Boudon,
474 V., Ismail, S.: Self- and air-broadened line shapes in the 2ν₃ P and R branches of ¹²CH₄. *J. Mol.*
475 *Spectrosc., Spectroscopy with Synchrotron Radiation* 315, 114–136.
476 <https://doi.org/10.1016/j.jms.2015.05.003>, 2015.
- 477 Dicke, R.H.: The Effect of Collisions upon the Doppler Width of Spectral Lines. *Phys. Rev.* 89, 472–473.
478 <https://doi.org/10.1103/PhysRev.89.472>, 1953.
- 479 Domysławska, J., Wójtewicz, S., Masłowski, P., Cygan, A., Bielska, K., Trawiński, R.S., Ciuryło, R., Lisak, D.: A
480 new approach to spectral line shapes of the weak oxygen transitions for atmospheric applications. *J. Quant.*
481 *Spectrosc. Radiat. Transf.* 169, 111–121. <https://doi.org/10.1016/j.jqsrt.2015.10.019>, 2016.
- 482 Drouin, B.J., Benner, D.C., Brown, L.R., Cich, M.J., Crawford, T.J., Devi, V.M., Guillaume, A., Hodges, J.T.,
483 Mlawer, E.J., Robichaud, D.J., Oyafuso, F., Payne, V.H., Sung, K., Wishnow, E.H., Yu, S.: Multispectrum
484 analysis of the oxygen A-band. *J. Quant. Spectrosc. Radiat. Transf., Satellite Remote Sensing and*
485 *Spectroscopy: Joint ACE-Odin Meeting, October 2015* 186, 118–138.
486 <https://doi.org/10.1016/j.jqsrt.2016.03.037>, 2017.

487 Gordon, I.E., Kassı, S., Campargue, A., Toon, G.C.: First identification of the electric quadrupole transitions of
488 oxygen in solar and laboratory spectra. *J. Quant. Spectrosc. Radiat. Transf.*, Special Issue Dedicated to
489 Laurence S. Rothman on the Occasion of his 70th Birthday. 111, 1174–1183.
490 <https://doi.org/10.1016/j.jqsrt.2010.01.008>, 2010.

491 Gordon, I.E., Rothman, L.S., Hill, C., Kochanov, R.V., Tan, Y., Bernath, P.F., Birk, M., Boudon, V., Campargue,
492 A., Chance, K.V., Drouin, B.J., Flaud, J.-M., Gamache, R.R., Hodges, J.T., Jacquemart, D., Perevalov, V.I.,
493 Perrin, A., Shine, K.P., Smith, M.-A.H., Tennyson, J., Toon, G.C., Tran, H., Tyuterev, V.G., Barbe, A.,
494 Császár, A.G., Devi, V.M., Furtenbacher, T., Harrison, J.J., Hartmann, J.-M., Jolly, A., Johnson, T.J.,
495 Karman, T., Kleiner, I., Kyuberis, A.A., Loos, J., Lyulin, O.M., Massie, S.T., Mikhailenko, S.N., Moazzen-
496 Ahmadi, N., Müller, H.S.P., Naumenko, O.V., Nikitin, A.V., Polyansky, O.L., Rey, M., Rotger, M.,
497 Sharpe, S.W., Sung, K., Starikova, E., Tashkun, S.A., Auwera, J.V., Wagner, G., Wilzewski, J., Wcislo, P.,
498 Yu, S., Zak, E.J.: The HITRAN2016 molecular spectroscopic database. *J. Quant. Spectrosc. Radiat.*
499 *Transf.*, HITRAN2016 Special Issue 203, 3–69. <https://doi.org/10.1016/j.jqsrt.2017.06.038>, 2017.

500 Griffith, D.W.T., Deutscher, N.M., Velazco, V.A., Wennberg, P.O., Yavin, Y., Keppel-Aleks, G., Washenfelder,
501 R.A., Toon, G.C., Blavier, J.-F., Paton-Walsh, C., Jones, N.B., Kettlewell, G.C., Connor, B.J., Macatangay,
502 R.C., Roehl, C., Ryzek, M., Glowacki, J., Culgan, T., Bryant, G.W.: TCCON data from Darwin (AU),
503 Release GGG2014.R0. <https://doi.org/10.14291/tcon.ggg2014.darwin01.R0/1149290>, 2017.

504 Hartmann, J.-M., Sironneau, V., Boulet, C., Svensson, T., Hodges, J.T., Xu, C.T.: Collisional broadening and
505 spectral shapes of absorption lines of free and nanopore-confined O₂ gas. *Phys. Rev. A* 87, 032510.
506 <https://doi.org/10.1103/PhysRevA.87.032510>, 2013.

507 Hill, C., Brown, J.M., Newnham, D.A.: An upper limit for the magnitude of pressure shifts in the O₂
508 a¹Δ_g←X³Σ_g⁻(0–0) band. *J. Mol. Spectrosc.* 221, 286–287. [https://doi.org/10.1016/S0022-2852\(03\)00227-3](https://doi.org/10.1016/S0022-2852(03)00227-3),
509 2003.

510 Hodges, J.T.: Automated high-resolution frequency-stabilized cavity ring-down absorption spectrometer. *Rev. Sci.*
511 *Instrum.* 76, 023112. <https://doi.org/10.1063/1.1850633>, 2005.

512 Hodges, J.T., Layer, H.P., Miller, W., Scace, G.E.: Frequency-stabilized single-mode cavity ring-down apparatus
513 for high-resolution absorption spectroscopy. *Rev. Sci. Instrum.* 75, 849–863.
514 <https://doi.org/10.1063/1.1666984>, 2004.

515 Keppel-Aleks, G., Toon, G.C., Wennberg, P.O., Deutscher, N.M.: Reducing the impact of source brightness
516 fluctuations on spectra obtained by Fourier-transform spectrometry. *Appl. Opt.* 46, 4774.
517 <https://doi.org/10.1364/AO.46.004774>, 2007.

518 Lamouroux, J., Sironneau, V., Hodges, J.T., Hartmann, J.-M.: Isolated line shapes of molecular oxygen:
519 Requantized classical molecular dynamics calculations versus measurements. *Phys. Rev. A* 89, 042504.
520 <https://doi.org/10.1103/PhysRevA.89.042504>, 2014.

521 Leshchishina, O., Kassı, S., Gordon, I.E., Rothman, L.S., Wang, L., Campargue, A.: High sensitivity CRDS of the
522 a¹Δ_g←X³Σ_g⁻ band of oxygen near 1.27 μm: Extended observations, quadrupole transitions, hot bands and
523 minor isotopologues. *J. Quant. Spectrosc. Radiat. Transf.*, XVIth Symposium on High Resolution
524 Molecular Spectroscopy (HighRus-2009) XVIth Symposium on High Resolution Molecular Spectroscopy
525 111, 2236–2245. <https://doi.org/10.1016/j.jqsrt.2010.05.014>, 2010.

526 Leshchishina, O., Kassı, S., Gordon, I.E., Yu, S., Campargue, A.: The band of ¹⁶O¹⁷O, ¹⁷O¹⁸O and ¹⁷O₂ by high
527 sensitivity CRDS near 1.27 μm. *J. Quant. Spectrosc. Radiat. Transf.* 112, 1257–1265.
528 <https://doi.org/10.1016/j.jqsrt.2011.01.014>, 2011.

529 Lévy, A., Lacombe, N., Chackerian Jr., C.: Collisional Line Mixing A2 - Weber, K. Narahari Rao Alfons, in:
530 Spectroscopy of the Earth's Atmosphere and Interstellar Medium. Academic Press, pp. 261–337, 1992.

531 Lin, H., Reed, Z.D., Sironneau, V.T., Hodges, J.T.: Cavity ring-down spectrometer for high-fidelity molecular
532 absorption measurements. *J. Quant. Spectrosc. Radiat. Transf.* 161, 11–20.
533 <https://doi.org/10.1016/j.jqsrt.2015.03.026>, 2015.

534 Lin, J.C., Gerbig, C., Wofsy, S.C., Daube, B.C., Matross, D.M., Chow, V.Y., Gottlieb, E., Andrews, A.E.,
535 Pathmathevan, M., Munger, J.W.: What have we learned from intensive atmospheric sampling field
536 programmes of CO₂? *Tellus B* 58, 331–343. <https://doi.org/10.1111/j.1600-0889.2006.00202.x>, 2006.

537 Long, D.A., Havey, D.K., Okumura, M., Miller, C.E., Hodges, J.T.: O₂ A-band line parameters to support
538 atmospheric remote sensing. *J. Quant. Spectrosc. Radiat. Transf.* 111, 2021–2036.
539 <https://doi.org/10.1016/j.jqsrt.2010.05.011>, 2010.

540 Maté, B., Lugez, C., Fraser, G.T., Lafferty, W.J.: Absolute intensities for the O₂ 1.27 μm continuum absorption. *J.*
541 *Geophys. Res. Atmospheres* 104, 30585–30590. <https://doi.org/10.1029/1999JD900824>, 1999.

542 Mendonca, J., Strong, K., Toon, G.C., Wunch, D., Sung, K., Deutscher, N.M., Griffith, D.W.T., Franklin, J.E.:
543 Improving atmospheric CO₂ retrievals using line mixing and speed-dependence when fitting high-
544 resolution ground-based solar spectra. *J. Mol. Spectrosc., Atmospheric Spectroscopy* 323, 15–27.
545 <https://doi.org/10.1016/j.jms.2016.01.007>, 2016.

546 Mertz, L.: Auxiliary computation for Fourier spectrometry. *Infrared Phys.* 7, 17–23. [https://doi.org/10.1016/0020-0891\(67\)90026-7](https://doi.org/10.1016/0020-0891(67)90026-7), 1967.

548 Messerschmidt, J., Macatangay, R., Notholt, J., Petri, C., Warneke, T., Weinzierl, C.: Side by side measurements of
549 CO₂ by ground-based Fourier transform spectrometry (FTS): SIDE BY SIDE MEASUREMENTS OF CO₂
550 BY FTS. *Tellus B* 62, 749–758. <https://doi.org/10.1111/j.1600-0889.2010.00491.x>, 2010.

551 Mlawer, E.J., Clough, S.A., Brown, P.D., Stephen, T.M., Landry, J.C., Goldman, A., Murcray, F.J.: Observed
552 atmospheric collision-induced absorption in near-infrared oxygen bands. *J. Geophys. Res. Atmospheres*
553 103, 3859–3863. <https://doi.org/10.1029/97JD03141>, 1998.

554 Newman, S.M., Lane, I.C., Orr-Ewing, A.J., Newnham, D.A., Ballard, J.: Integrated absorption intensity and
555 Einstein coefficients for the O₂ a¹Δ_g-X³Σ_g⁻ (0,0) transition: A comparison of cavity ringdown and high
556 resolution Fourier transform spectroscopy with a long-path absorption cell. *J. Chem. Phys.* 110, 10749–
557 10757. <https://doi.org/10.1063/1.479018>, 1999.

558 Newman, S.M., Orr-Ewing, A.J., Newnham, D.A., Ballard, J.: Temperature and pressure dependence of line widths
559 and integrated absorption intensities for the O₂ a¹Δ_g - X³Σ_g⁻ (0,0) transition. *J. Phys. Chem. A* 104, 9467–
560 9480, 2000.

561 Ngo, N.H., Lisak, D., Tran, H., Hartmann, J.-M.: An isolated line-shape model to go beyond the Voigt profile in
562 spectroscopic databases and radiative transfer codes. *J. Quant. Spectrosc. Radiat. Transf.* 129, 89–100.
563 <https://doi.org/10.1016/j.jqsrt.2013.05.034>, 2013.

564 Predoi-Cross, A., Hambrook, K., Keller, R., Povey, C., Schofield, I., Hurtmans, D., Over, H., Mellau, G.C.:
565 Spectroscopic lineshape study of the self-perturbed oxygen A-band. *J. Mol. Spectrosc.* 248, 85–110.
566 <https://doi.org/10.1016/j.jms.2007.11.007>, 2008.

567 Rohart, F., Mäder, H., Nicolaisen, H.-W.: Speed dependence of rotational relaxation induced by foreign gas
568 collisions: Studies on CH₃F by millimeter wave coherent transients. *J. Chem. Phys.* 101, 6475–6486.
569 <https://doi.org/10.1063/1.468342>, 1994.

570 Rothman, L.S., Gordon, I.E., Babikov, Y., Barbe, A., Chris Benner, D., Bernath, P.F., Birk, M., Bizzocchi, L.,
571 Boudon, V., Brown, L.R., Campargue, A., Chance, K., Cohen, E.A., Coudert, L.H., Devi, V.M., Drouin,
572 B.J., Fayt, A., Flaud, J.-M., Gamache, R.R., Harrison, J.J., Hartmann, J.-M., Hill, C., Hodges, J.T.,
573 Jacquemart, D., Jolly, A., Lamouroux, J., Le Roy, R.J., Li, G., Long, D.A., Lyulin, O.M., Mackie, C.J.,
574 Massie, S.T., Mikhailenko, S., Müller, H.S.P., Naumenko, O.V., Nikitin, A.V., Orphal, J., Perevalov, V.,
575 Perrin, A., Polovtseva, E.R., Richard, C., Smith, M.A.H., Starikova, E., Sung, K., Tashkun, S., Tennyson,
576 J., Toon, G.C., Tyuterev, V.G., Wagner, G.: The HITRAN2012 molecular spectroscopic database. *J. Quant.*
577 *Spectrosc. Radiat. Transf., HITRAN2012 special issue* 130, 4–50.
578 <https://doi.org/10.1016/j.jqsrt.2013.07.002>, 2013.

579 Rothman, L.S., Gordon, I.E., Barbe, A., Benner, D.C., Bernath, P.F., Birk, M., Boudon, V., Brown, L.R.,
580 Campargue, A., Champion, J.-P., Chance, K., Coudert, L.H., Dana, V., Devi, V.M., Fally, S., Flaud, J.-M.,
581 Gamache, R.R., Goldman, A., Jacquemart, D., Kleiner, I., Lacombe, N., Lafferty, W.J., Mandin, J.-Y.,
582 Massie, S.T., Mikhailenko, S.N., Miller, C.E., Moazzen-Ahmadi, N., Naumenko, O.V., Nikitin, A.V.,
583 Orphal, J., Perevalov, V.I., Perrin, A., Predoi-Cross, A., Rinsland, C.P., Rotger, M., Šimečková, M., Smith,
584 M.A.H., Sung, K., Tashkun, S.A., Tennyson, J., Toth, R.A., Vandaele, A.C., Vander Auwera, J.: The
585 HITRAN 2008 molecular spectroscopic database. *J. Quant. Spectrosc. Radiat. Transf., HITRAN* 110, 533–
586 572. <https://doi.org/10.1016/j.jqsrt.2009.02.013>, 2009.

587 Rothman, L.S., Jacquemart, D., Barbe, A., Chris Benner, D., Birk, M., Brown, L.R., Carleer, M.R., Chackerian Jr.,
588 C., Chance, K., Coudert, L.H., Dana, V., Devi, V.M., Flaud, J.-M., Gamache, R.R., Goldman, A.,
589 Hartmann, J.-M., Jucks, K.W., Maki, A.G., Mandin, J.-Y., Massie, S.T., Orphal, J., Perrin, A., Rinsland,
590 C.P., Smith, M.A.H., Tennyson, J., Tolchenov, R.N., Toth, R.A., Vander Auwera, J., Varanasi, P., Wagner,
591 G.: The HITRAN 2004 molecular spectroscopic database. *J. Quant. Spectrosc. Radiat. Transf.* 96, 139–204.
592 <https://doi.org/10.1016/j.jqsrt.2004.10.008>, 2005.

593 Shannon, I., Harris, M., McHugh, D.R., Lewis, E.L.: Low-pressure spectral line profiles: an analysis in terms of
594 symmetric speed-dependent Voigt profiles. *J. Phys. B At. Mol. Phys.* 19, 1409.
595 <https://doi.org/10.1088/0022-3700/19/10/011>, 1986.

596 Singh, H.B., Brune, W.H., Crawford, J.H., Jacob, D.J., Russell, P.B.: Overview of the summer 2004 Intercontinental
597 Chemical Transport Experiment-North America (INTEX-A). *J. Geophys. Res. Atmospheres* 111, D24S01.
598 <https://doi.org/10.1029/2006JD007905>, 2006.

599 Smith, K.M., Newnham, D.A.: Near-infrared absorption cross sections and integrated absorption intensities of
600 molecular oxygen (O₂, O₂-O₂, and O₂-N₂). *J. Geophys. Res. Atmospheres* 105, 7383–7396.
601 <https://doi.org/10.1029/1999JD901171>, 2000.

602 Smith, K.M., Newnham, D.A., Williams, R.G.: Collision-induced absorption of solar radiation in the atmosphere by
603 molecular oxygen at 1.27 μm: Field observations and model calculations. *J. Geophys. Res. Atmospheres*
604 106, 7541–7552. <https://doi.org/10.1029/2000JD900699>, 2001.

605 Strong, K., Mendonca, J., Weaver, D., Fogal, P., Drummond, J.R., Batchelor, R., Lindenmaier, R.: TCCON data
606 from Eureka (CA), Release GGG2014.R1. <https://doi.org/10.14291/tcon.ggg2014.eureka01.R1/1325515>,
607 2017.

608 Toon, G. C.: Telluric line list for GGG2014, TCCON data archive. Carbon Dioxide Inf. Anal. Cent. Oak Ridge Natl.
609 Lab. Oak Ridge Tenn. USA. <https://doi.org/10.14291/tcon.ggg2014.atm.R0/1221656>, 2014a.

610 Toon, G. C.: Solar line list for GGG2014. TCCON Data Arch. Hosted Carbon Dioxide Inf. Anal. Cent. Oak Ridge
611 Natl. Lab. Oak Ridge Tenn. USA, 2014b.

612 Toon, G.C.: The JPL MkIV interferometer. *Opt. Photonics News* 2, 19–21.
613 <https://doi.org/10.1364/OPN.2.10.000019>, 1991.

614 Tran, H., Boulet, C., Hartmann, J.-M.: Line mixing and collision-induced absorption by oxygen in the A band:
615 Laboratory measurements, model, and tools for atmospheric spectra computations. *J. Geophys. Res.*
616 *Atmospheres* 111, D15210. <https://doi.org/10.1029/2005JD006869>, 2006.

617 Tran, H., Hartmann, J.-M.: An improved O₂ A band absorption model and its consequences for retrievals of photon
618 paths and surface pressures. *J. Geophys. Res. Atmospheres* 113, D18104.
619 <https://doi.org/10.1029/2008JD010011>, 2008.

620 Tran, H., Ngo, N.H., Hartmann, J.-M.: Efficient computation of some speed-dependent isolated line profiles. *J.*
621 *Quant. Spectrosc. Radiat. Transf.* 129, 199–203. <https://doi.org/10.1016/j.jqsrt.2013.06.015>, 2013.

622 Wallace, L., Livingston, W.: Spectroscopic observations of atmospheric trace gases over Kitt Peak. I - Carbon
623 dioxide and methane from 1979 to 1985. *J. Geophys. Res.* 95, 9823–9827.
624 <https://doi.org/10.1029/JD095iD07p09823>, 1990.

625 Washenfelder, R.A., Toon, G.C., Blavier, J.-F., Yang, Z., Allen, N.T., Wennberg, P.O., Vay, S.A., Matross, D.M.,
626 Daube, B.C.: Carbon dioxide column abundances at the Wisconsin Tall Tower site. *J. Geophys. Res.*
627 *Atmospheres* 111, D22305. <https://doi.org/10.1029/2006JD007154>, 2006.

628 Wehr, R.A.: Dicke -narrowed spectral lines in carbon monoxide buffered by argon (Ph.D.). University of Toronto
629 (Canada), Canada, 2005.

630 Wennberg, P.O., Roehl, C.M., Wunch, D., Toon, G.C., Blavier, J.-F., Washenfelder, R., Keppel-Aleks, G., Allen,
631 N.T., Ayers, J.: TCCON data from Park Falls (US), Release GGG2014.R0.
632 <https://doi.org/10.14291/tcon.ggg2014.parkfalls01.R0/1149161>, 2017a.

633 Wennberg, P.O., Wunch, D., Roehl, C.M., Blavier, J.-F., Toon, G.C., Allen, N.T., Dowell, P., Teske, K., Martin, C.,
634 Martin, J.: TCCON data from Lamont (US), Release GGG2014.R0.
635 <https://doi.org/10.14291/tcon.ggg2014.lamont01.R0/1149159>, 2017b.

636 Wofsy, S.C.: HIAPER Pole-to-Pole Observations (HIPPO): fine-grained, global-scale measurements of climatically
637 important atmospheric gases and aerosols. *Philos. Trans. R. Soc. Lond. Math. Phys. Eng. Sci.* 369, 2073–
638 2086. <https://doi.org/10.1098/rsta.2010.0313>, 2011.

639 Wójtewicz, S., Cygan, A., Masłowski, P., Domysławska, J., Lisak, D., Trawiński, R.S., Ciuryło, R.: Spectral line
640 shapes of self-broadened P-branch transitions of oxygen B band. *J. Quant. Spectrosc. Radiat. Transf.* 144,
641 36–48. <https://doi.org/10.1016/j.jqsrt.2014.03.029>, 2014.

642 Wunch, D., Toon, G.C., Blavier, J.-F.L., Washenfelder, R.A., Notholt, J., Connor, B.J., Griffith, D.W.T., Sherlock,
643 V., Wennberg, P.O.: The Total Carbon Column Observing Network. *Philos. Trans. R. Soc. Math. Phys.*
644 *Eng. Sci.* 369, 2087–2112. <https://doi.org/10.1098/rsta.2010.0240>, 2011.

645 Wunch, D., Toon, G.C., Sherlock, V., Deutscher, N.M., Liu, C., Feist, D.G., Wennberg, P.O.: The Total Carbon
646 Column Observing Network’s GGG2014 Data Version.
647 <https://doi.org/10.14291/tcon.ggg2014.documentation.R0/1221662>, 2015.

648 Wunch, D., Toon, G.C., Wennberg, P.O., Wofsy, S.C., Stephens, B.B., Fischer, M.L., Uchino, O., Abshire, J.B.,
649 Bernath, P., Biraud, S.C., Blavier, J.-F.L., Boone, C., Bowman, K.P., Browell, E.V., Campos, T., Connor,
650 B.J., Daube, B.C., Deutscher, N.M., Diao, M., Elkins, J.W., Gerbig, C., Gottlieb, E., Griffith, D.W.T.,
651 Hurst, D.F., Jiménez, R., Keppel-Aleks, G., Kort, E.A., Macatangay, R., Machida, T., Matsueda, H.,

652 Moore, F., Morino, I., Park, S., Robinson, J., Roehl, C.M., Sawa, Y., Sherlock, V., Sweeney, C., Tanaka,
653 T., Zondlo, M.A.: Calibration of the Total Carbon Column Observing Network using aircraft profile data.
654 Atmos Meas Tech 3, 1351–1362. <https://doi.org/10.5194/amt-3-1351-2010>, 2010.
655 Yang, Z., Toon, G.C., Margolis, J.S., Wennberg, P.O.: Atmospheric CO₂ retrieved from ground-based near IR solar
656 spectra. Geophys. Res. Lett. 29, 1339. <https://doi.org/10.1029/2001GL014537>, 2002.
657 Yokota, T., Yoshida, Y., Eguchi, N., Ota, Y., Tanaka, T., Watanabe, H., Maksyutov, S.: Global Concentrations of
658 CO₂ and CH₄ Retrieved from GOSAT: First Preliminary Results. Sola 5, 160–163.
659 <https://doi.org/10.2151/sola.2009-041>, 2009.
660 Yu, S., Drouin, B.J., Miller, C.E.: High resolution spectral analysis of oxygen. IV. Energy levels, partition sums,
661 band constants, RKR potentials, Franck-Condon factors involving the X³Σ_g⁻, a¹Δ_g and b¹Σ_g⁺ states. J.
662 Chem. Phys. 141, 174302. <https://doi.org/10.1063/1.4900510>, 2014.
663

664

665

666

667

668

669

670

671

672

673

674

675

676

677

678

679

680

681

682

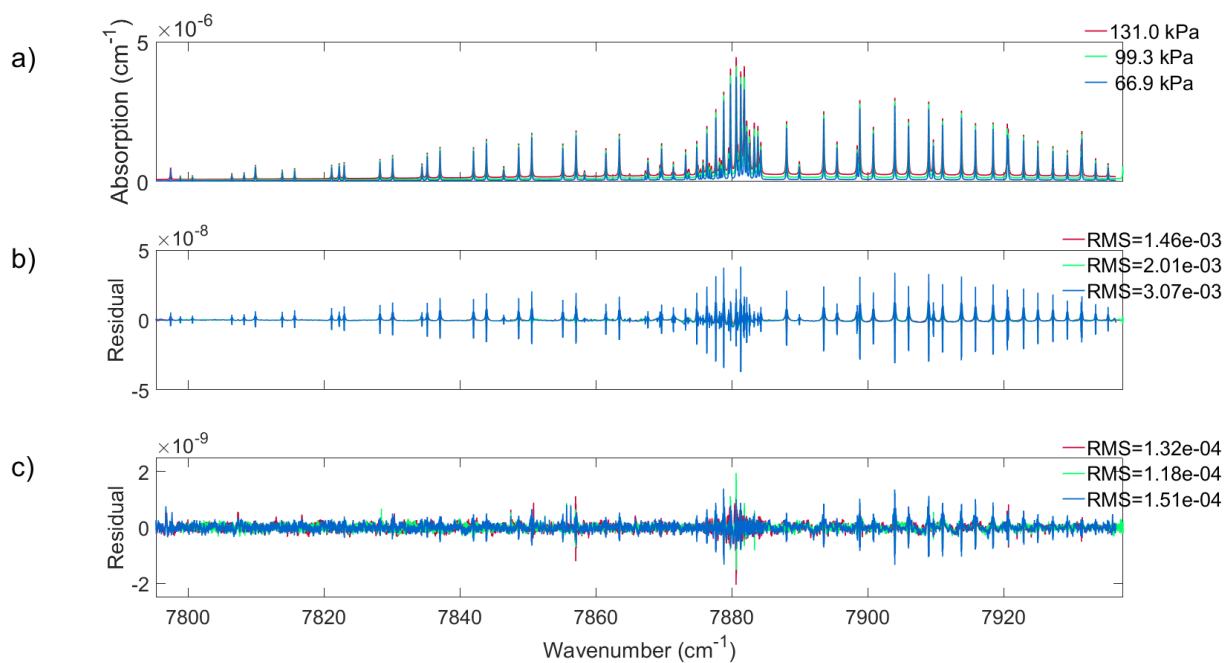
683

684

685

686

687 **Figures**



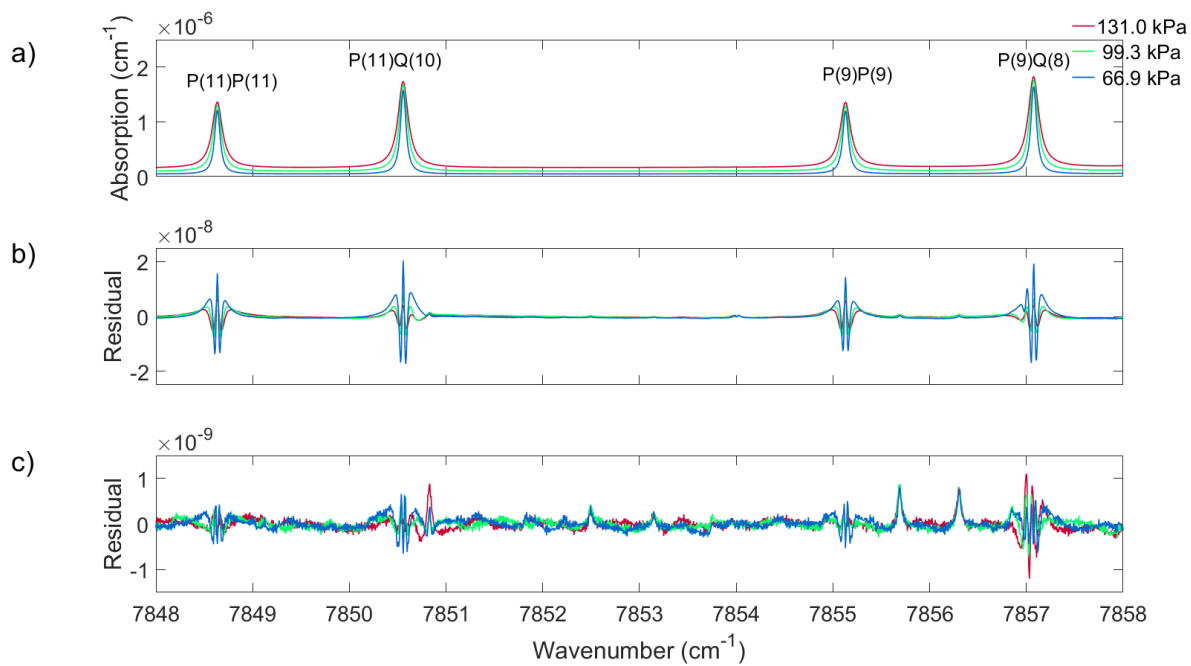
688

689 **Figure 1: (a) Cavity-ring-down absorption coefficients for O₂ measured at the three pressures indicated in the**
690 **legend at approximately room temperature and a volume mixing ratio of 0.20720(43). The difference between**
691 **measured absorption coefficients and those calculated using (b) a Voigt line shape, and (c) the speed-**
692 **dependent Voigt line shape. Note the difference in scale between panels (b) and (c).**

693

694

695



696

697 **Figure 2: The same as Figure 1 but expanded to show four spectral lines in the P branch of the O₂ 1.27 μm**
 698 **band.**

699

700

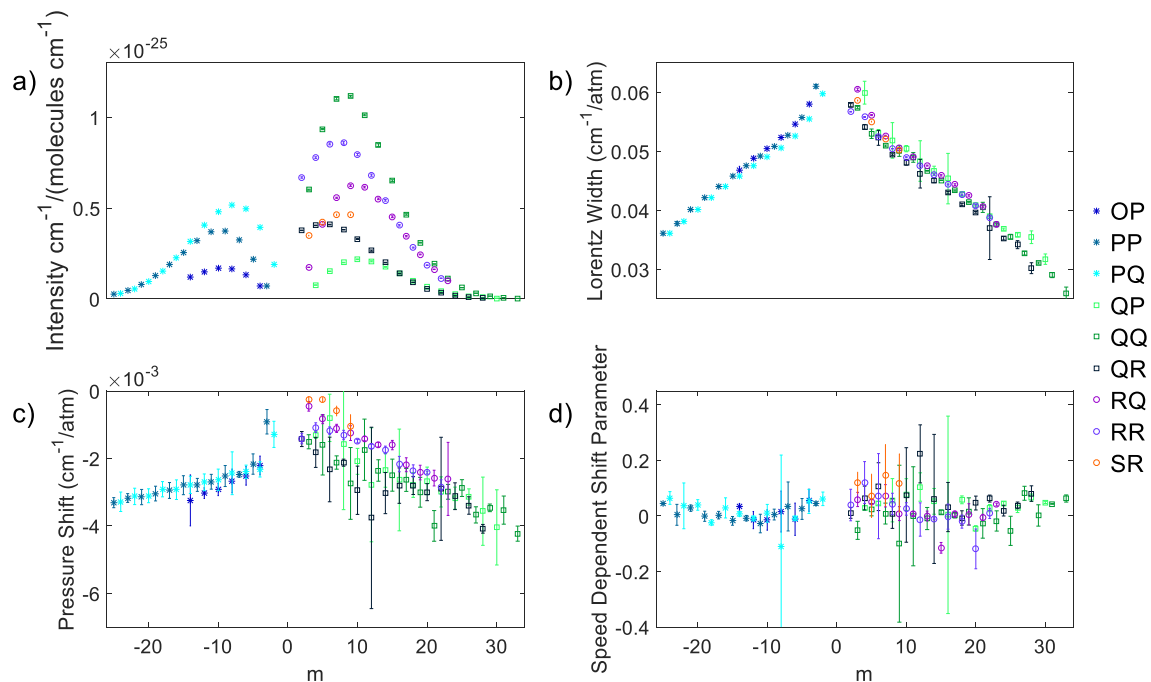
701

702

703

704

705



706

707 **Figure 3: The averaged measured (a) intensity, (b) Lorentz line width, (c) pressure shift, and (d) speed-**
 708 **dependent pressure shift retrieved from the three cavity ring-down spectra of the 1.27 μm band of O_2 . All**
 709 **data are plotted as a function of m which is $m=-J$ for the P-branch lines, $m=J$ for the Q-branch, and $m=J+1$**
 710 **for the R-branch (where J is the lower state rotational quantum number) and the uncertainties shown are 2σ .**

711

712

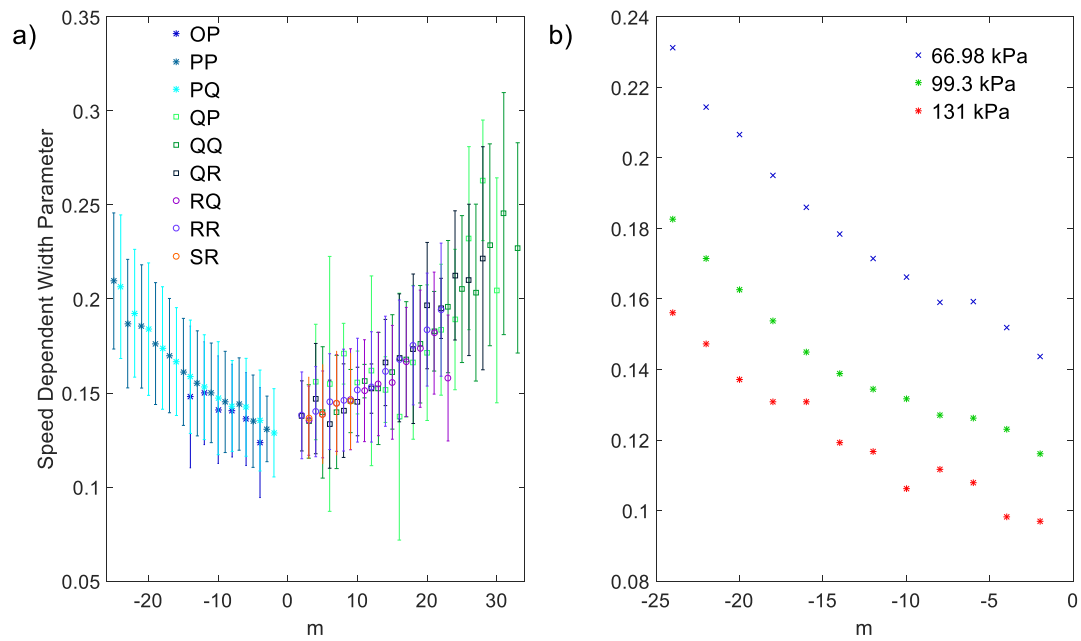
713

714

715

716

717



718

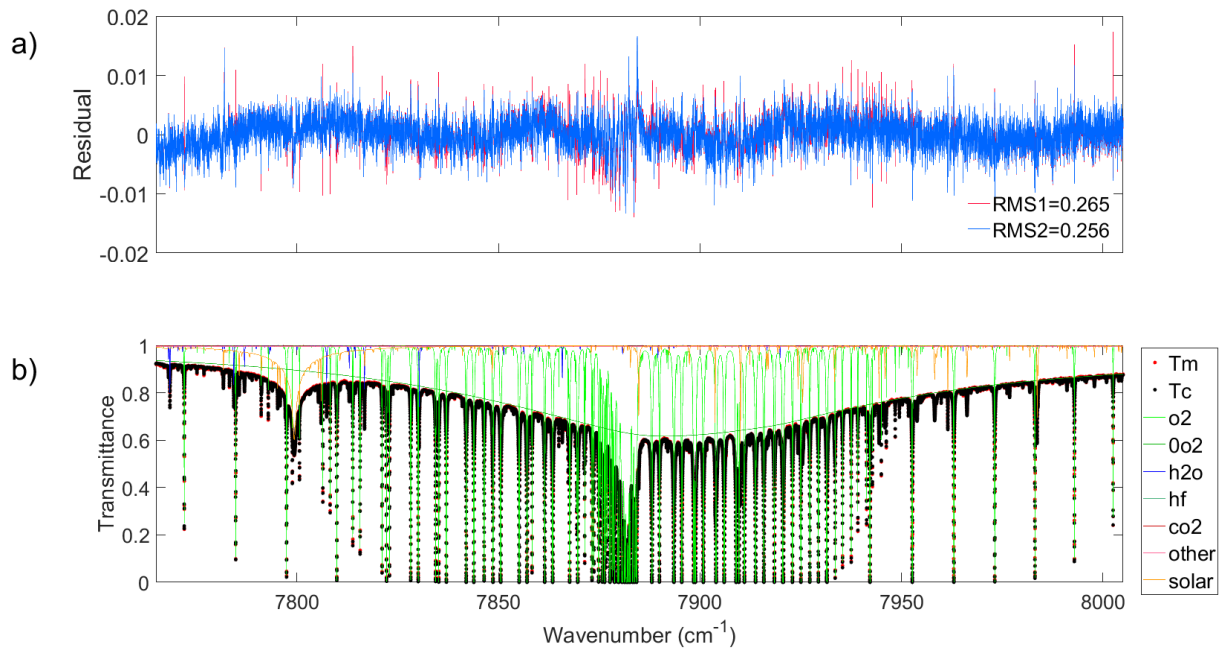
719 **Figure 4: (a) The averaged measured speed-dependent width parameter of the 1.27 μm band of O_2 plotted as**
 720 **a function of m. (b) The measured speed-dependent width parameter for spectral lines that belong to the PQ**
 721 **sub-branch plotted as a function of m.**

722

723

724

725



726

727 **Figure 5: (a) The residuals (measured minus calculated) for a spectrum measured at Eureka on March 27,**
 728 **2015 at a SZA of 81.32°. The red residual is the result of using the Voigt line shape and the blue is from using**
 729 **the qSDV. (b) The measured (red dots) and calculated (black dots), with the qSDV, spectrum, along with the**
 730 **gases included in the fit (refer to the legend to the right) in the spectral window.**

731

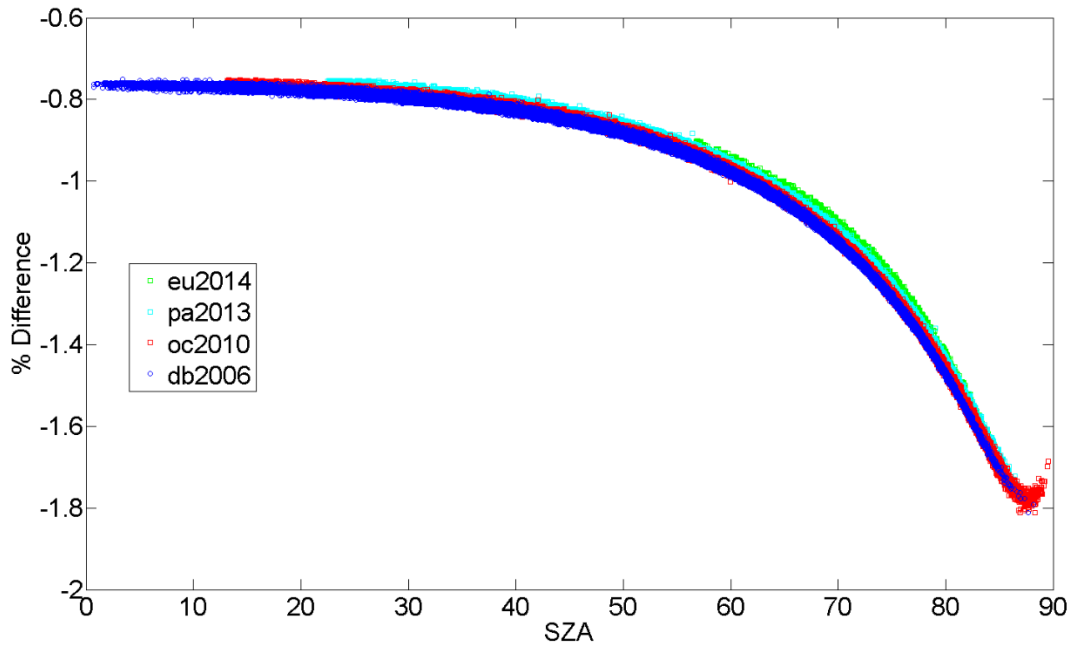
732

733

734

735

736



737

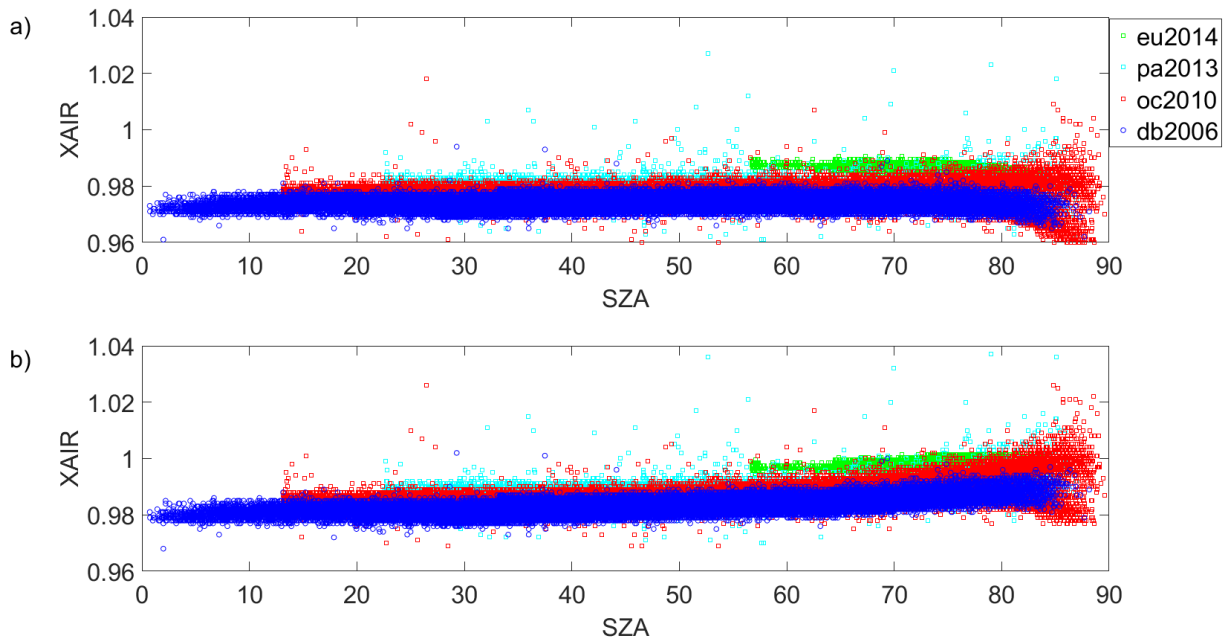
738 **Figure 6: The percent difference between the O₂ column retrieved with the Voigt and qSDV line shapes for a**
739 **year of measurements from Eureka (eu), Park Falls (pa), Lamont (oc), and Darwin (db).**

740

741

742

743



744

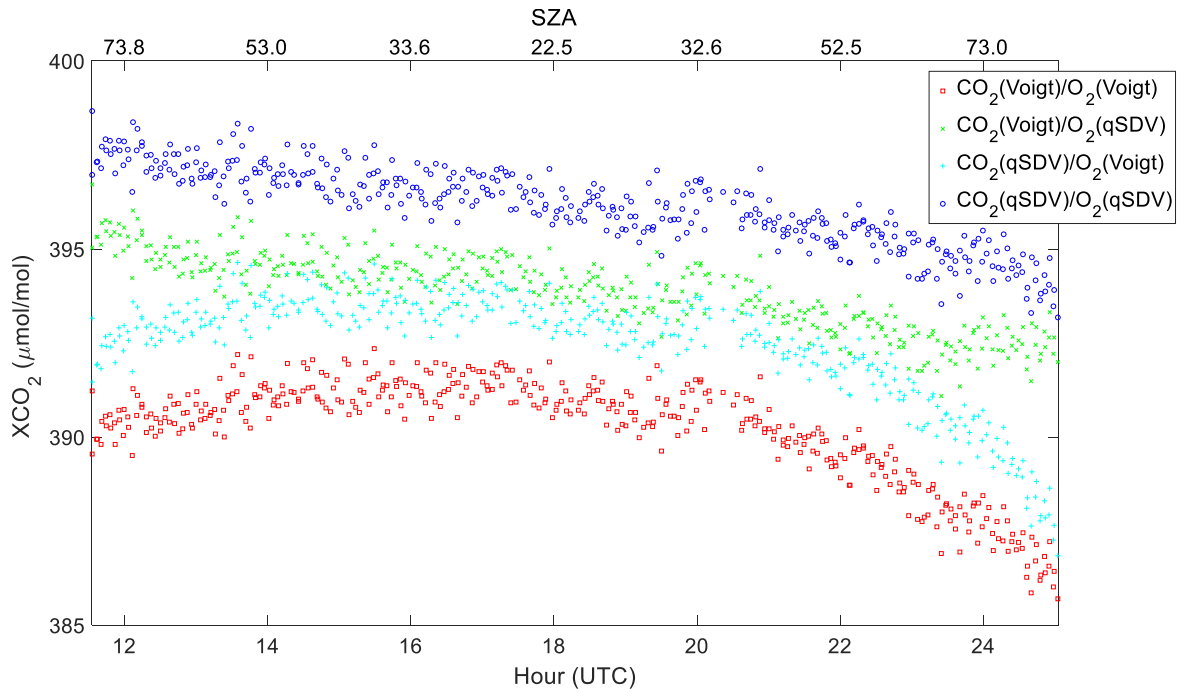
745 **Figure 7: (a) XAIR as a function of SZA calculated using the total column of O₂ retrieved using the Voigt line**
 746 **shape. (b) is the same as (a) except the total column of O₂ was retrieved with the qSDV.**

747

748

749

750

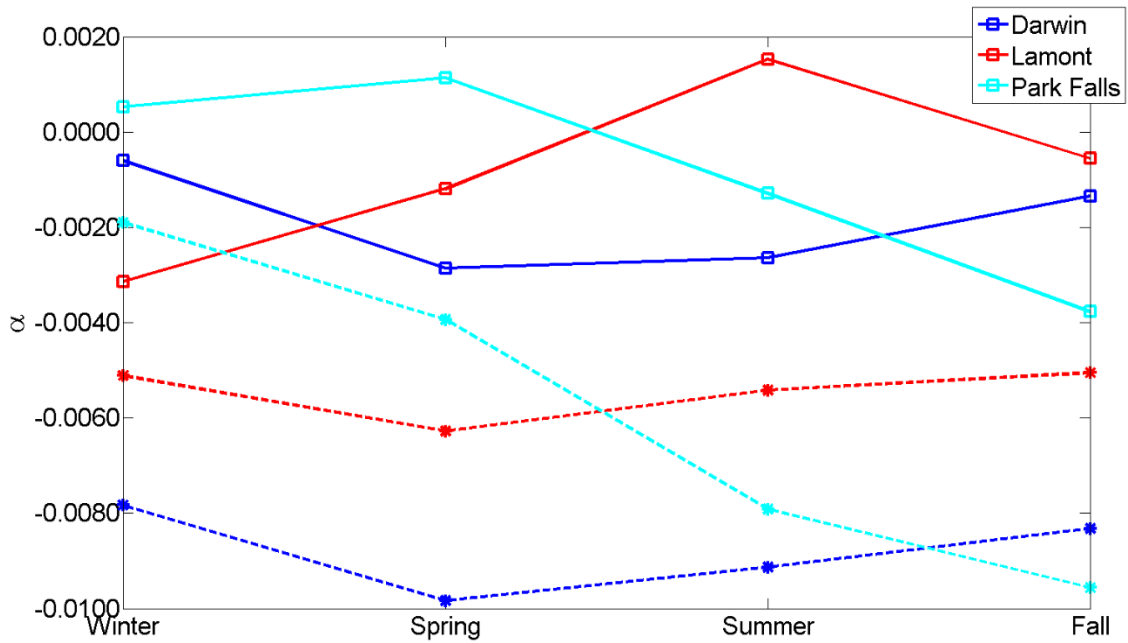


751

752 **Figure 8: XCO₂ calculated from the CO₂ and O₂ columns retrieved from Park Falls spectra recorded on June**
 753 **18, 2013. The CO₂ columns were retrieved using either the Voigt line shape or the qSDV with line mixing,**
 754 **while the O₂ columns were retrieved using either the Voigt or qSDV line shapes. XCO₂ was calculated in**
 755 **four ways: 1) Both CO₂ and O₂ columns retrieved using the Voigt line shape (red), 2) CO₂ columns retrieved**
 756 **with the Voigt and O₂ columns retrieved with the qSDV (green), 3) CO₂ columns retrieved with the qSDV**
 757 **and line mixing and O₂ columns retrieved with the Voigt (cyan), and 4) CO₂ columns retrieved with the qSDV**
 758 **and line mixing and O₂ columns retrieved with the qSDV (blue). The top x-axis is the SZA that corresponds**
 759 **to the hour on the bottom x-axis.**

760

761



762

763 **Figure 9:** The average air mass-dependent correction factor for XCO₂ derived from a year of spectra
 764 measured at Darwin, Lamont, and Park Falls for different seasons. The dashed lines with stars are the α for
 765 XCO₂ retrieved using a Voigt line shape for both CO₂ and O₂ columns. The solid lines with squares are from
 766 XCO₂ retrieved using the qSDV for both CO₂ and O₂ columns.

767

768

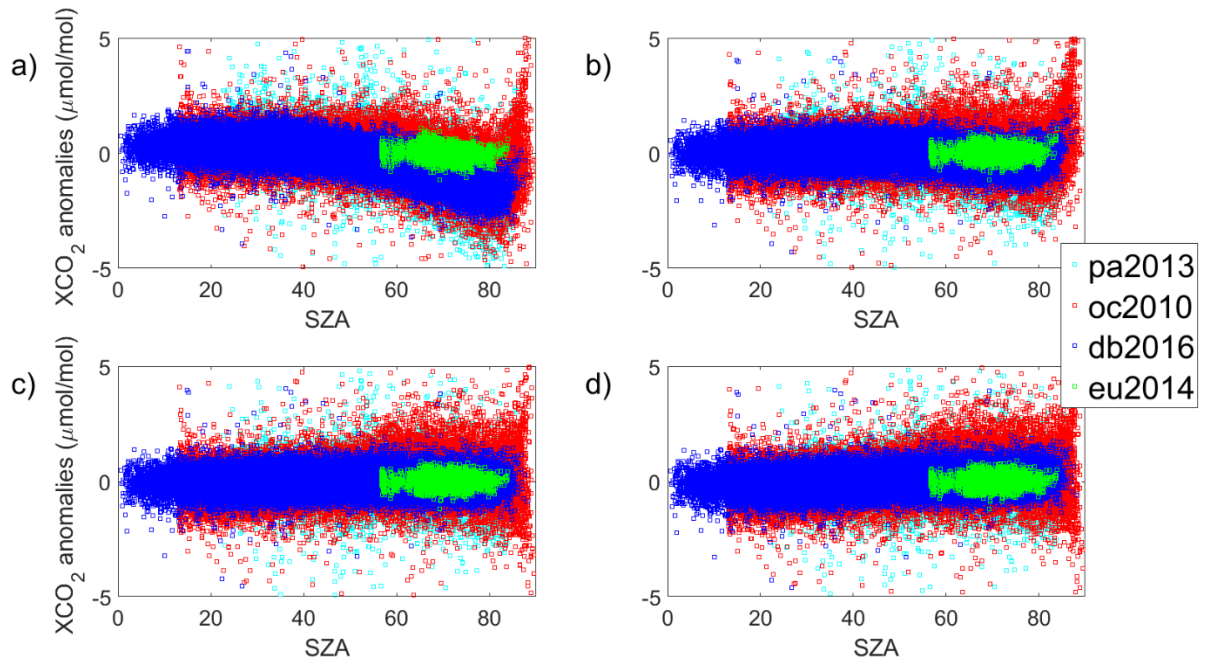
769

770

771

772

773



774

775 **Figure 10: (a) XCO₂ Voigt anomaly for a year of measurements from the four TCCON sites. The XCO₂**
 776 **anomaly is the difference between each XCO₂ value and the daily median XCO₂. (b) The XCO₂ Voigt**
 777 **anomaly after the airmass dependence correction is applied to the XCO₂ Voigt data. (c) XCO₂ qSDV**
 778 **anomaly. (d) XCO₂ qSDV anomaly after correction for the airmass dependence.**

779

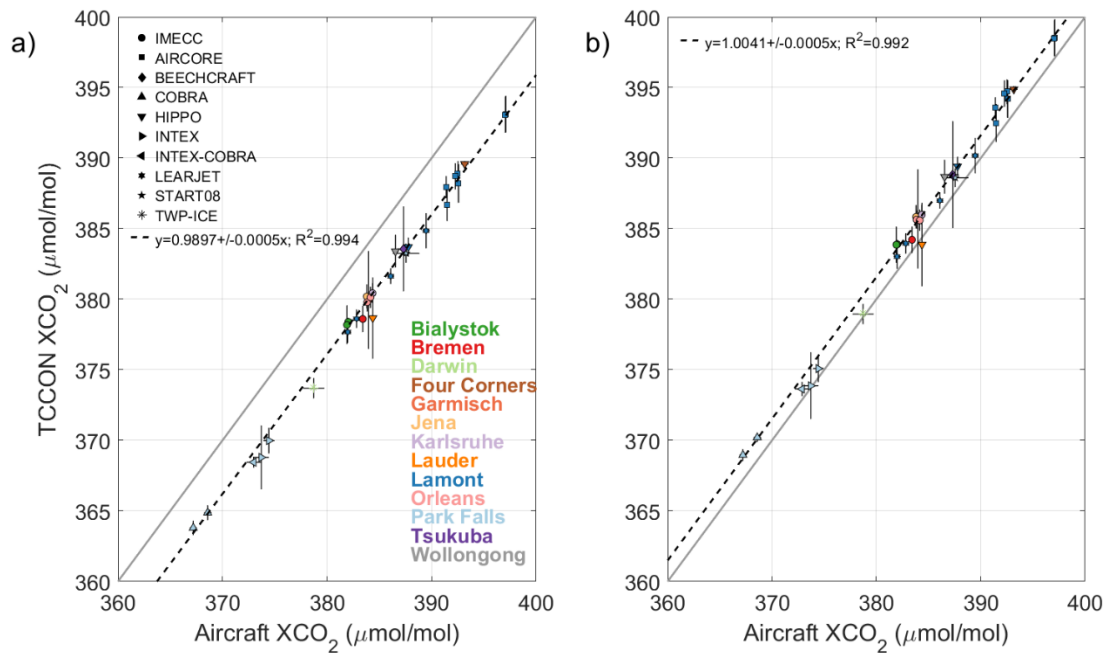
780

781

782

783

784



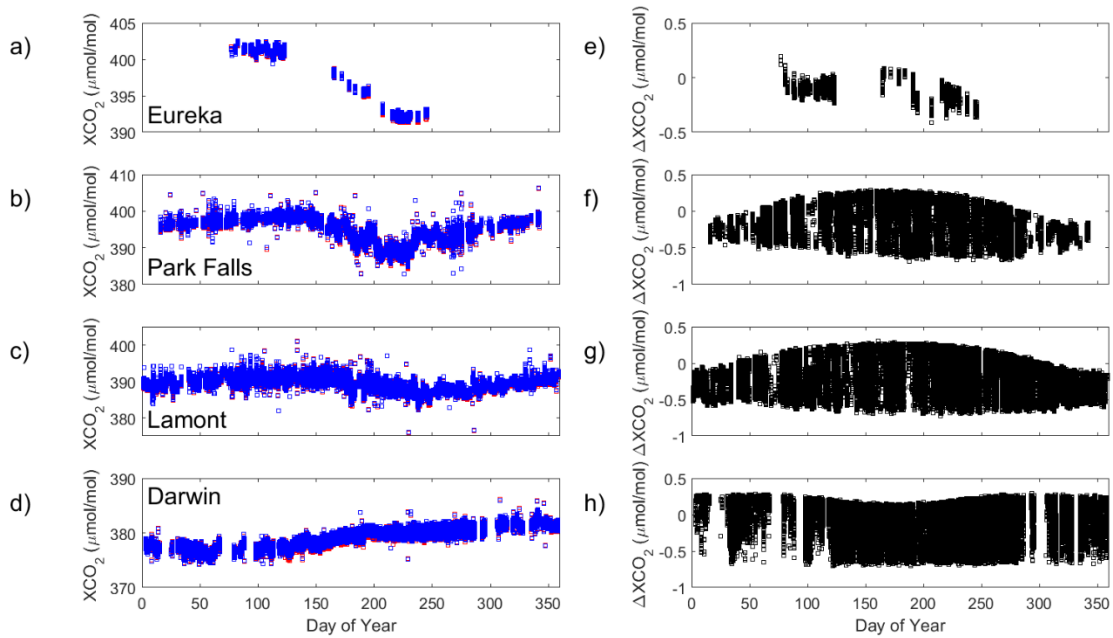
785

786 **Figure 11: (a) Correlation between TCCON and aircraft XCO₂ Voigt measurements for 13 TCCON sites.**
 787 **Each aircraft type is indicated by a different symbol given by the legend in the top left corner. Each site is**
 788 **represented by a different colour given by the legend in the bottom right corner. The grey line indicates the**
 789 **one-to-one line and the dashed line is the line of best fit for the data. The slope of the line of best fit as well as**
 790 **the error on the slope are given in the plot. (b) the same as (a) but for XCO₂ qSDV.**

791

792

793



794

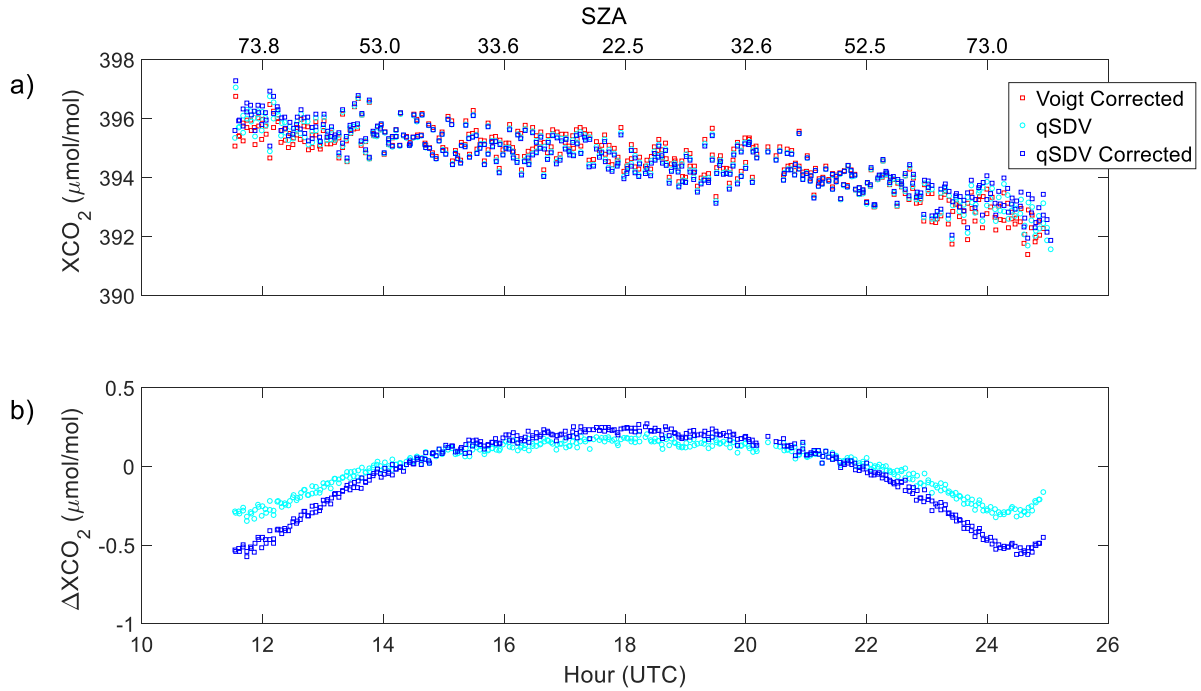
795 **Figure 12: (a) to (d) XCO₂ plotted as a function of day of the year for Eureka (2014), Park Falls (2013),**
 796 **Lamont (2010), and Darwin (2006) respectively. The mostly-hidden red boxes are XCO₂ calculated from**
 797 **using a Voigt line shape in the retrieval and the blue boxes are from using the qSDV. (e) to (h) the difference**
 798 **between XCO₂ Voigt and XCO₂ qSDV.**

799

800

801

802



803

804 **Figure 13: (a) XCO₂ from Park Falls retrieved from spectra recorded on June 18, 2013. Plotted is XCO₂**
805 **retrieved: (1) with a Voigt line shape and corrected for the airmass dependence (red squares), (2) with the**
806 **qSDV (cyan circles), and (3) with the qSDV and corrected for the airmass dependence (blue squares). (b) the**
807 **difference between the Voigt XCO₂ corrected and the qSDV XCO₂ (cyan circles), and the difference between**
808 **the Voigt XCO₂ corrected and the qSDV XCO₂ corrected (blue squares). The top x-axis is the SZA that**
809 **corresponds to the hour on the bottom x-axis.**

810